Soft Matter

PAPER

View Article Online
View Journal | View Issue

Cite this: *Soft Matter*, 2021, **17**, 2539

Kinetics of self-assembly of inclusions due to lipid membrane thickness interactions

Xinyu Liao [a] and Prashant K. Purohit *[ab]

Received 30th September 2020,
Accepted 19th January 2021

DOI: 10.1039/d0sm01752c

rsc.li/soft-matter-journal

Self-assembly of proteins on lipid membranes underlies many important processes in cell biology, such as, exo- and endo-cytosis, assembly of viruses, *etc.* An attractive force that can cause self-assembly is mediated by membrane thickness interactions between proteins. The free energy profile associated with this attractive force is a result of the overlap of thickness deformation fields around the proteins which can be calculated from the solution of a boundary value problem. Yet, the time scales over which two inclusions coalesce has not been explored, even though the evolution of particle concentrations on membranes has been modeled using phase-field approaches. In this paper we compute this time scale as a function of the initial distance between two inclusions by viewing their coalescence as a first passage time problem. The mean first passage time is computed using Langevin dynamics and a partial differential equation, and both methods are found to be in excellent agreement. Inclusions of three different shapes are studied and it is found that for two inclusions separated by about hundred nanometers the time to coalescence is hundreds of milliseconds irrespective of shape. An efficient computation of the interaction energy of inclusions is central to our work. We compute it using a finite difference technique and show that our results are in excellent agreement with those from a previously proposed semi-analytical method based on Fourier–Bessel series. The computational strategies described in this paper could potentially lead to efficient methods to explore the kinetics of self-assembly of proteins on lipid membranes.

1 Introduction

Self-assembly of proteins on lipid membranes has been a topic of interest for at least the last three decades.[1–3] Proteins on membranes self-assemble because they interact with each other through forces that have their origins in membrane bending deformations,[4,5] membrane thickness deformations,[4,6–11] electrostatics[12] and entropic interactions.[4,13] There is a large literature on this topic that we do not attempt to review here.[3–6,13–20] Our interest is in self-assembly caused by membrane thickness mediated interactions of proteins.

It is well known that lipid bilayers consist of two leaflets with the hydrophobic tails of the lipid molecules spanning the membrane thickness. Proteins that are embedded in the membrane have hydrophobic peptides placed in such a way as they interact mostly with the hydrophobic tails of the lipid molecules. If the thickness of the hydrophobic region of a protein is different from that of the lipid membrane then the leaflets deform so that the membrane thickness in the vicinity of the protein changes (see Fig. 1). The energy cost of the thickness deformation has been estimated analytically by taking account of the lipid hydrocarbon chain entropy.[9,21] The result is an energy functional written in terms of the deformation field $u(x,y)$ of the half-membrane thickness and its gradients.[4,9] The membrane bending modulus K_b, the membrane thickness modulus K_t and the isotropic membrane tension F enter as parameters into this functional. The Euler–Lagrange equation obtained by the minimization of this energy functional is a fourth order linear partial differential equation (PDE). A series of papers by Phillips, Klug, Haselwandter and colleagues[6–8] start from this energy functional and utilize the linearity of the PDE to computationally analyze allosteric interactions of clusters of proteins of various shapes. The key idea is that the thickness deformation fields caused by distant proteins can overlap (superimpose) and give rise to interaction forces just as defects in elastic solids interact due to the overlap of deformation fields.[22] This idea has been in place since at least the mid-1990s,[9] but it was computationally extended to complex protein shapes and large clusters by the above authors.

An important result that emerged from the research on clusters discussed above[6] is that the free energy has a maximum when plotted as a function of distance between individual proteins which form a lattice (the proteins on the lattice are

[a] *Graduate Group in Applied Mathematics and Computational Science, University of Pennsylvania, Philadelphia, PA 19104, USA. E-mail: xinyul@sas.upenn.edu, purohit@seas.upenn.edu*
[b] *Department of Mechanical Engineering and Applied Mechanics, University of Pennsylvania, Philadelphia, PA 19104, USA*

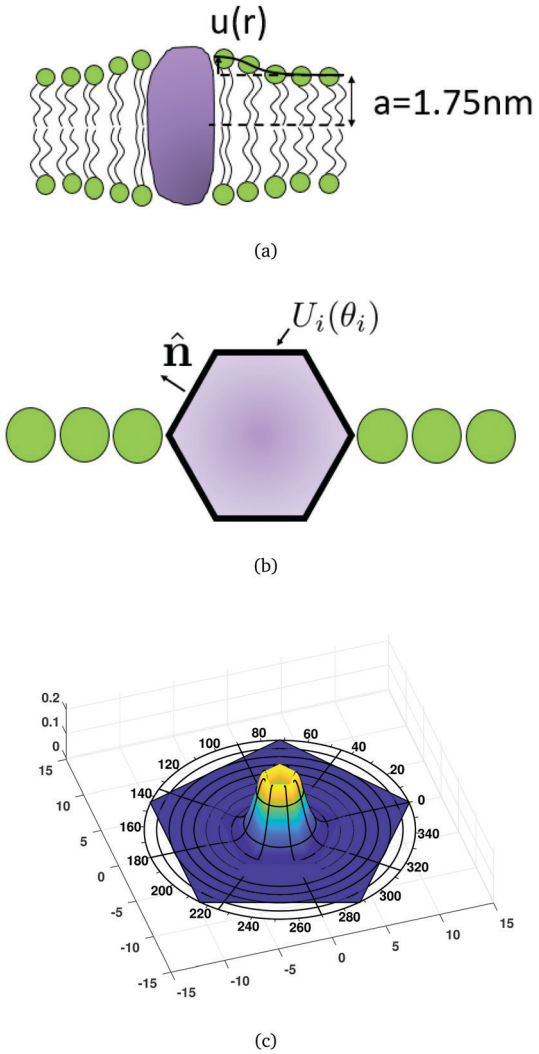

Fig. 1 (a) Schematic of bilayer deformations due to a thickness mismatch between hydrophobic region of a bilayer leaflet and an embedded protein. (b) The two types of boundary conditions that are used in this work. Dirichlet boundary condition $U_i(\theta_i)$ gives the thickness deformation along the boundary of inclusion i, while the slope boundary condition $\nabla u \cdot \hat{\mathbf{n}} = U_i'(\theta_i)$ determines the derivative along normal directions at each point along the boundary of inclusion i. The top view of the surrounding lipid molecules (green circles) is only shown along the horizontal line, but the lipids are everywhere on the plane. (c) A 3d plot of the thickness deformation field caused by one hexagonal inclusion. The thickness deformation is significant in the immediate vicinity of the inclusion and decays rapidly as one moves further away.

all identical). To the left of the maximum there are strong attractive interactions between the proteins, while to the right there are weak repulsive forces which decay away as the proteins move far apart. The strong attractive forces should cause self-assembly if two (or more) proteins happen to come close together as they diffuse on the membrane. We are interested in the time scale of the self-assembly process. There are few experiments which focus on this time scale, but one by Shnyrova *et al.*[23] found that viral proteins (that did not interact electrostatically) on a micron-sized vesicle self-assemble in seconds.

Temporal evolution of the self-assembly of viral proteins on a lipid membrane has been analyzed in a few recent papers using simulations. Often these simulations can be computationally prohibitive, but they do give insight about time scales and intermediate states of the cluster of proteins assembling into a virus particle or nano-container.[1–3,24] A drawback of these simulations is that they may not be able to tackle time scales of seconds over which self-assembly was seen to occur in experiments.[23] There is a large literature on phase-field approaches that can capture the evolution of particle concentrations on membranes (see for example ref. 25 and 26), but these methods are not appropriate for computing the time to coalescence of a few particles diffusing on a membrane. We will take a different approach in this paper by analyzing self-assembly of differently shaped inclusions using Langevin dynamics and the corresponding Fokker–Planck equations. In recent work we viewed self-assembly of two inclusions as a first-passage time problem which can be quantitatively analyzed using the theory of stochastic processes.[27] We implemented this approach in the context of interactions based on membrane bending. The analytical calculations (using PDEs) in ref. 27 were confined to absorbing boundary conditions on both boundaries. A novelty of this work is that we extend the PDE approach to include absorbing and reflecting boundary conditions.

This paper is arranged as follows. First, we quantify the interaction energy profile of hexagonal, rod- and star-shaped inclusions.† We show that our finite difference numerical method for computing energies agrees very well with analytical formulae (using Fourier–Bessel series) in most cases. After computing the interaction energies, we solve first-passage time problems to find the time scales over which two inclusions coalesce due to attractive interactions. We use both Langevin dynamics and the Fokker–Planck equation to obtain mean first passage times and study both isotropic and anisotropic problems with reflecting/absorbing boundary conditions. Finally, we summarize our results in the discussion and conclusion sections and point to various enrichments that can be implemented following our earlier work.[27]

2 Energy landscape

2.1 Analytical solution based on Fourier–Bessel basis

We consider a circular lipid membrane with radius R_2 and two inclusions embedded in it. Our first goal is to compute the energy landscape seen by an inclusion interacting with another inclusion on a flat membrane. The interactions between the inclusions are a result of the overlap of membrane thickness deformation fields in their vicinity (see Fig. 1(c) for the thickness deformation profile around one inclusion). The interaction energy will be computed by considering two inclusions, one fixed and the other moving as shown in Fig. 2(a). The coordinate frame at the fixed inclusion (blue) denoted as inclusion 1 (r_1,θ_1)

† We are limited in the shapes we can explore by the equilateral triangle grid used in our computations.

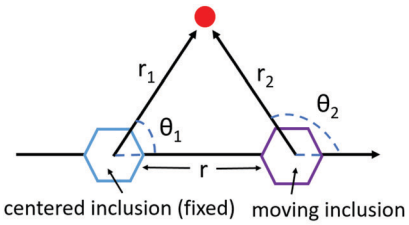

(a)

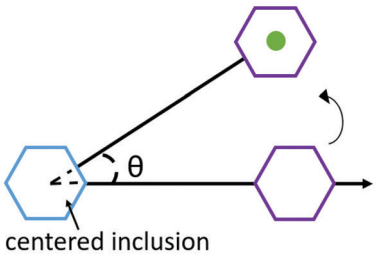

(b)

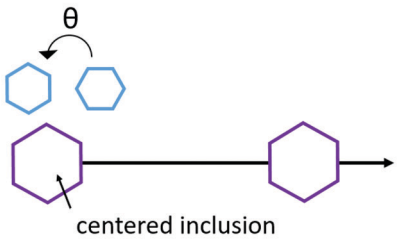

(c)

Fig. 2 (a) The initial configuration of a system of two inclusions. The fixed inclusion located at the center (blue) has local coordinate system (r_1,θ_1) and the moving inclusion (purple) has local coordinate system (r_2,θ_2). (b) The inclusion on the right moves to the green spot and forms an angle θ with the horizontal line. (c) The energy of the configuration here is the same as the one in (b). Note that the hexagons in (c) are rotated when compared to hexagons in (a).

is set to be the default one. We assume that the moving inclusion (purple) denoted as inclusion 2 initially stays in the same orientation as inclusion 1 (see Fig. 2(a)). To keep the analysis simple, when an inclusion moves we do not consider its rotational diffusion (see ref. 27 where rotational diffusion was considered). As inclusion 2 moves from its initial position to the green spot and forms an angle θ with the horizontal line (see Fig. 2(b)), the energy of the system can be computed by rotating both inclusions anticlockwise by angle θ from the initial configuration (see Fig. 2(c)). This interaction energy will enter our analysis of the kinetics of the moving inclusion due to Brownian motion.

The elastic energy due to thickness deformation is given by,[6–8,10]

$$\phi = \frac{1}{2}\int\left\{K_b(\nabla^2 u)^2 + K_t\left(\frac{u}{a}\right)^2 + F\left[\frac{2u}{a} + (\nabla u)^2\right]\right\}\mathrm{d}x\mathrm{d}y, \quad (1)$$

where K_b is the membrane bending modulus, K_t is the thickness deformation modulus, F is the applied tension and a is the unperturbed bilayer half-thickness. The integration is carried out over the area of the membrane. The Euler–Lagrange equation associated with eqn (1) is given by,[7]

$$K_b\nabla^4 u - F\nabla^2 u + \frac{K_t}{a^2}u + \frac{F}{a} = 0. \quad (2)$$

Eqn (2) can be reduced to the following form using the transformation $\bar{u} = u + \frac{Fa}{K_t}$,

$$\begin{aligned}(\nabla^2 - \nu_+)(\nabla^2 - \nu_-)\bar{u} &= 0,\\ \nu_\pm &= \frac{1}{2K_b}\left[F \pm \left(F^2 - \frac{4K_bK_t}{a^2}\right)^{\frac{1}{2}}\right].\end{aligned} \quad (3)$$

First, we consider the case of an infinitely large circular membrane with $R_2 \to \infty$ without applied tension ($F = 0$). We assume natural boundary condition which means that $u = \bar{u} \to 0$ as $R_2 \to \infty$. Let inclusion 2 be on the right side of inclusion 1. Then, a Fourier–Bessel series solution for the thickness deformation field around each inclusion $i(i = 1,2)$ can be obtained,

$$\begin{aligned}\bar{u}_i^{\pm}(r_i,\theta_i) &= A_{i,0}^{\pm}K_0(\sqrt{\nu_\pm}r_i) + \sum_{n=1}^{\infty}A_{i,n}^{\pm}K_n(\sqrt{\nu_\pm}r_i)\cos n\theta_i\\ &\quad + B_{i,n}^{\pm}K_n(\sqrt{\nu_\pm}r_i)\sin n\theta_i\\ &\approx A_{i,0}^{\pm}K_0(\sqrt{\nu_\pm}r_i) + \sum_{n=1}^{N}A_{i,n}^{\pm}K_n(\sqrt{\nu_\pm}r_i)\cos n\theta_i\\ &\quad + B_{i,n}^{\pm}K_n(\sqrt{\nu_\pm}r_i)\sin n\theta_i,\end{aligned} \quad (4)$$

where K_n are modified Bessel functions of the second kind and we take the first N terms in the series to approximate the sum. In ref. 8 the authors used $N = 12$ to compute energy caused by thickness deformations and they showed that the series is almost converged. For small applied tension F and large membrane size R_2, we follow ref. 8 and use eqn (4) as an approximation for the solution of $\bar{u}_i^{\pm}$.‡ Since the Euler–Lagrange equation (eqn (2)) is linear, the solution for eqn (3) is given by,[8]

$$\bar{u} = \bar{u}_1^{+}(r_1,\theta_1) + \bar{u}_1^{-}(r_1,\theta_1) + \bar{u}_2^{+}(r_2,\theta_2) + \bar{u}_2^{-}(r_2,\theta_2), \quad (5)$$

in which we used the coordinate transformations,

$$\begin{aligned}r_2 &= \sqrt{r^2 + r_1^2 - 2rr_1\cos\theta_1} \triangleq \mathscr{F}_1(r_1,\cos\theta_1,r),\\ \cos\theta_2 &= (-r + r_1\cos\theta_1)/r_2, \quad \sin\theta_2 = r_1\sin\theta_1/r_2;\\ r_1 &= \sqrt{r^2 + r_2^2 + 2rr_2\cos\theta_2} \triangleq \mathscr{F}_2(r_2,\cos\theta_2,r),\\ \cos\theta_1 &= (r + r_2\cos\theta_2)/r_1, \quad \sin\theta_1 = r_2\sin\theta_2/r_1.\end{aligned} \quad (6)$$

In order to efficiently apply the boundary conditions, we rewrite

‡ The solution should include terms of the modified Bessel functions of the first kind when $F \neq 0$ and R_2 is finite. However, we show later that this approximation agrees quite well with the numerical solution of eqn (2).

$\bar{u}_2$ as a function of r_1,θ_1,r and $\bar{u}_1$ as a function of r_2,θ_2,r,

$$\begin{aligned}\hat{u}_1^{\pm}(r_2,\theta_2,r) &= A_{1,0}^{\pm}K_0(\sqrt{\nu_{\pm}}\mathscr{F}_2(r_2,\cos\theta_2,r))\\ &+ \sum_{n=1}^{N}A_{1,n}^{\pm}K_n(\sqrt{\nu_{\pm}}\mathscr{F}_2(r_2,\cos\theta_2,r))\\ &\times T_n\left(\frac{r}{r_1}+\frac{r_2}{r_1}\cos\theta_2\right)+\sum_{n=1}^{N}B_{1,n}^{\pm}K_n(\sqrt{\nu_{\pm}}\mathscr{F}_2\\ &\times (r_2,\cos\theta_2,r))U_{n-1}\left(\frac{r}{r_1}+\frac{r_2}{r_1}\cos\theta_2\right)\\ &\times \frac{r_2}{r_1}\sin\theta_2,\end{aligned} \tag{7}$$

$$\begin{aligned}\hat{u}_2^{\pm}(r_1,\theta_1,r) &= A_{2,0}^{\pm}K_0(\sqrt{\nu_{\pm}}\mathscr{F}_1(r_1,\cos\theta_1,r))\\ &+ \sum_{n=1}^{N}A_{2,n}^{\pm}K_n(\sqrt{\nu_{\pm}}\mathscr{F}_1(r_1,\cos\theta_1,r))\\ &\times T_n\left(-\frac{r}{r_2}+\frac{r_1}{r_2}\cos\theta_1\right)+\sum_{n=1}^{N}B_{2,n}^{\pm}K_n\\ &\times (\sqrt{\nu_{\pm}}\mathscr{F}_1(r_1,\cos\theta_1,r))U_{n-1}\left(-\frac{r}{r_2}+\frac{r_1}{r_2}\cos\theta_1\right)\\ &\times \frac{r_1}{r_2}\sin\theta_1,\end{aligned} \tag{8}$$

where T_n, U_n are Chebyshev polynomials of the first kind and second kind, respectively. Let $h_1=\bar{u}_1^{+}+\bar{u}_1^{-}$, $h_2=\bar{u}_2^{+}+\bar{u}_2^{-}$, $\hat{h}_1=\hat{u}_1^{+}+\hat{u}_1^{-}$, $\hat{h}_2=\hat{u}_2^{+}+\hat{u}_2^{-}$. We consider the following type of boundary conditions (see Fig. 1(b)),

$$\begin{aligned}(h_1+\hat{h}_2)(\mathscr{R}_1(\theta_1),\theta_1,r) &= U_1(\theta_1)\\ \hat{\mathbf{n}}\cdot\left(\frac{\partial(h_1+\hat{h}_2)}{\partial r_1},\frac{1}{r_1}\frac{\partial(h_1+\hat{h}_2)}{\partial\theta_1}\right)(\mathscr{R}_1(\theta_1),\theta_1,r) &= U_1'(\theta_1)\end{aligned} \tag{9}$$

$$\begin{aligned}(\hat{h}_1+h_2)(\mathscr{R}_2(\theta_2),\theta_2,r) &= U_2(\theta_2)\\ \hat{\mathbf{n}}\cdot\left(\frac{\partial(\hat{h}_1+h_2)}{\partial r_2},\frac{1}{r_2}\frac{\partial(\hat{h}_1+h_2)}{\partial\theta_2}\right)(\mathscr{R}_2(\theta_2),\theta_2,r) &= U_2'(\theta_2).\end{aligned} \tag{10}$$

We can solve for the $4(2N+1)$ coefficients $A_{1,0}^{\pm}$, $A_{2,0}^{\pm}$, $A_{1,n}^{\pm}$, $A_{2,n}^{\pm}$, $B_{1,n}^{\pm}$, $B_{2,n}^{\pm}$, $n=1,2,\ldots,N$ because eqn (9) and (10) result in a linear system. This determines the full deformation field due to the overlap of the deformations caused by both inclusions. In the above expressions $\mathscr{R}_1$ is the shape function for inclusion 1 which is defined as the boundary of inclusion 1 in the polar coordinates (r_1,θ_1), and similarly for $\mathscr{R}_2$ which is the shape function of inclusion 2. For a hexagon shaped inclusion $\mathscr{R}_1$ is given by

$$\mathscr{R}_1=\frac{\sqrt{3}\ell}{2}\csc\left(\theta_1-\frac{\pi}{3}\left(-1+\operatorname{floor}\left(\frac{3\theta_1}{\pi}\right)\right)\right),\quad 0<\theta_1\le 2\pi, \tag{11}$$

where ℓ is the side length. The shape functions for rod shaped inclusion and star shaped inclusion are long and are given in the Appendix in the section named Shape functions for star and rod inclusion. The next step is to compute the energy $\phi(\mathbf{r})$ due to this deformation field. Note that the angular dependence of $\phi(\mathbf{r})$ appears through the shape functions of two inclusions, $\mathscr{R}_1$,$\mathscr{R}_2$.

Using the divergence theorem, the total energy expression in eqn (1) can be converted to the sum of line integrals over the boundary, *i.e.* $\phi=\phi_1+\phi_2$ with ϕ_i given by,

$$\begin{aligned}\phi_i &= \frac{1}{2}G_0+\frac{1}{2}\int\nabla\cdot\left[K_b(\nabla\bar{u})\nabla^2\bar{u}-K_b\bar{u}\nabla^3\bar{u}+F\bar{u}\nabla\bar{u}\right]\mathrm{d}x\mathrm{d}y\\ &= \frac{1}{2}G_1-\frac{1}{2}\int_0^{2\pi}\hat{\mathbf{n}}\cdot\left[K_b(\nabla\bar{u})\nabla^2\bar{u}-K_b\bar{u}\nabla^3\bar{u}+F\bar{u}\nabla\bar{u}\right]\\ &\quad\times\sqrt{\mathscr{R}_i^2(\theta_i)+\mathscr{R}_i'^2(\theta_i)}\mathrm{d}\theta_i\\ &= \frac{1}{2}G_1-\frac{1}{2}\int_0^{2\pi}\left[U_i'(\theta)(K_b(\nu_+\bar{u}_++\nu_-\bar{u}_-)+F\bar{u})\right.\\ &\quad\left.-K_b\bar{u}\hat{\mathbf{n}}\cdot\nabla(\nu_+\bar{u}_++\nu_-\bar{u}_-)\right]\sqrt{\mathscr{R}_i^2(\theta_i)+\mathscr{R}_i'^2(\theta_i)}\mathrm{d}\theta_i.\end{aligned} \tag{12}$$

From the first line to the second line we assume the line integral along the outer boundary is a constant w.r.t r (which works out to 0 as $R_2\to\infty$ and $F\to 0$) and put it into the G_1 term (both G_0 and G_1 are constants). To compute eqn (12) we need to solve for the $4(2N+1)$ coefficients $A_{1,0}^{\pm}$, $A_{2,0}^{\pm}$, $A_{1,n}^{\pm}$, $A_{2,n}^{\pm}$, $B_{1,n}^{\pm}$, $B_{2,n}^{\pm}$, $n=1,2,\ldots,N$ from eqn (9) and (10) and use them to compute $\bar{u}_+,\bar{u}_-$. Then we can evaluate eqn (12) numerically. The energy $\phi(\mathbf{r})$ can be computed relatively efficiently using this technique. This is important since $\phi(\mathbf{r})$ must be computed repeatedly as inclusion 2 moves and $\mathbf{r}$ changes due to Brownian motion when we solve the first passage time problem. We will also need the forces acting on inclusion 2 in our analysis later. Eqn (12) gives an expression to compute the force analytically, which in the special case of an isotropic $\phi(\mathbf{r})$ (*i.e.*, no angular dependence) works out to

$$\begin{aligned}\phi_i'(r) &= -\frac{R_i}{2}\int_0^{2\pi}\left[U_i'(\theta)\left(K_b(\nu_+\bar{u}_+'+\nu_-\bar{u}_-')+F\bar{u}'\right)\right.\\ &\quad\left.-K_b\bar{u}'\hat{\mathbf{n}}\cdot\nabla(\nu_+\bar{u}_++\nu_-\bar{u}_-)-K_b\bar{u}\hat{\mathbf{n}}\cdot\nabla(\nu_+\bar{u}_+'+\nu_-\bar{u}_-')\right]\mathrm{d}\theta_i.\end{aligned} \tag{13}$$

When there is only one circular inclusion in the membrane, the thickness deformation field in eqn (5) has a closed form solution[7] which can be compared to the simulation result of Klingelhoefer *et al.*[28] who studied radial bilayer thickness profiles for the $G\alpha$ nanopore (among many others). We used the same parameters and boundary conditions as they did: a = 34.19 Å, U_1 = 0.81 Å, $U_1'=0.7$, $\mathscr{R}_1$ = 10 Å for all θ_1 and fit their curves by choosing K_t = 120 pN nm^{-1}, K_b = 2 pN nm and F = 0. The black curve in Fig. 3(a) (which comes from eqn (4) with N = 8) captures the overall trend and the magnitude of the bilayer thickness changes in the simulation done by Kingelhoefer *et al.*[28] This is reasonable given that (a) the black curve is the

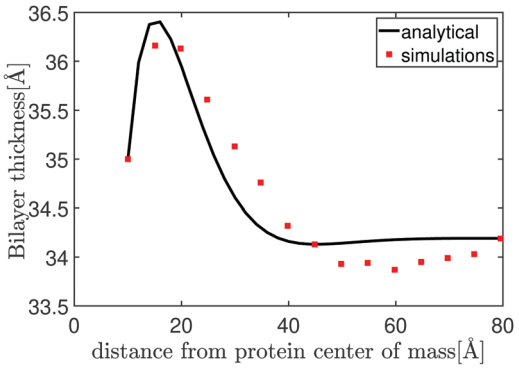

(a)

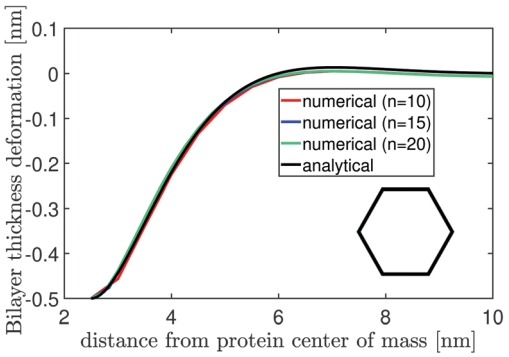

(b)

Fig. 3 (a) Red squares are data from the simulation done by Klingelhoefer *et al.*[28] and the black curve is fitted using the analytical method based on Fourier–Bessel function eqn (4). A reasonable agreement of the two profiles suggests that the energy functional eqn (1) and the associated Euler–Lagrange equation are a good starting point for estimating interaction energies of inclusions. (b) The thickness deformation of one hexagon inclusion with shape function eqn (11), K_b = 20 k_BT, K_t = 60 k_BT nm^{-2}, boundary conditions U_1 = −0.5 nm, $U_1' = 0$ and under applied tension F = 1 pN nm^{-1} converges to the result computed by analytical method eqn (4) with N = 8 as n increases. Recall that the side of the triangles in the fine grid is 1/n the side in the coarse grid.

result of a continuum approximation eqn (1) where as the lipids are discrete particles in the simulations of Kingelhoefer *et al.*,[28] and (b) the black curve assumes that the membrane is infinitely large where as it is finite in the simulations.

2.2 Finite difference method based on refined grid

The above analysis gives us a semi-analytical technique to compute $\phi(\mathbf{r})$. This technique can be used when there are one or two inclusions whose shapes are simple. For a larger number of inclusions or those with complex shapes (see Fig. 4(a)) we need a numerical method to compute the thickness deformation field. Fortunately, eqn (1) can be minimized using a finite difference method. We discretize the membrane using equilateral triangle elements as shown in Fig. 4(a) and (b) following.[29,30] We use a fine grid in the center of the domain and a coarse grid farther away for reasons explained below. Recall that one inclusion is fixed at the center of the domain and the other inclusion is allowed to move. The motion of the second inclusion is influenced by the change in interaction

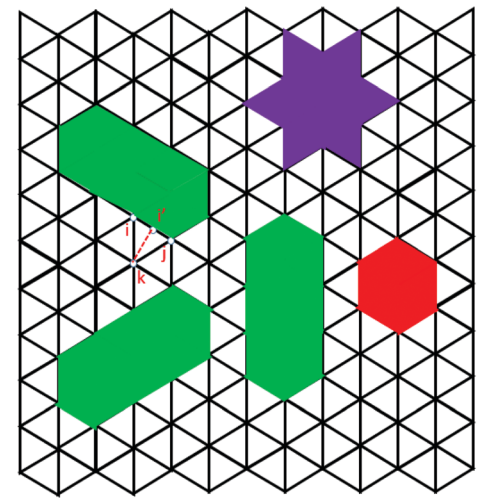

(a)

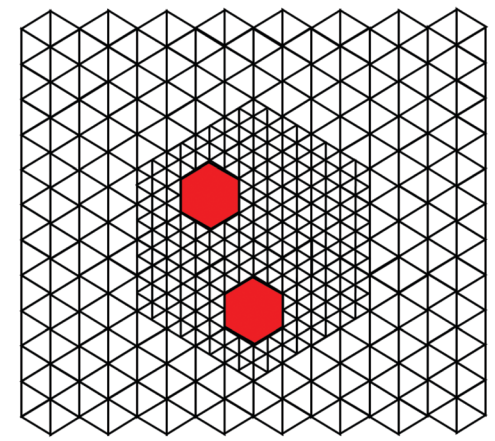

(b)

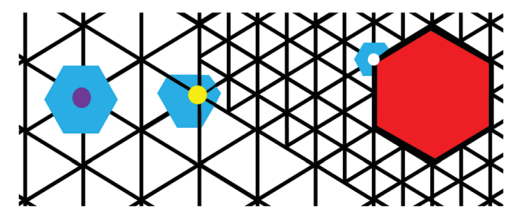

(c)

Fig. 4 (a) Triangular discretization of the membrane in our finite difference method. The side of the triangles is ℓ. Three types of inclusions are studied in this paper: hexagon (red), star (purple), rod (green). (b) A fine grid is implemented in a region near the center of the domain because the thickness deformation profile changes rapidly in that vicinity when two inclusions are present. The side of the triangles in the fine grid is 1/n that of the coarse grid. In this figure n = 2. (c) The blue regions are the Voronoi cells of purple node (in the coarse grid), yellow node (at the interface between fine and coarse grids) and white node (at the boundary of an inclusion), respectively.

energy between the inclusions. This interaction energy depends on the gradients of $u(x,y)$ which changes rapidly when the two inclusions are nearby (which happens when the second inclusion is near the center of the domain). Hence, to accurately compute the energy when the two inclusions are nearby

(see Fig. 4(b)) we use a fine grid in the center of the domain. When the inclusions are far away from each other there is hardly any interaction between them, so we use a coarse grid far away from the center of the domain to reduce computational cost. The side of the triangles in the fine grid is $1/n$ of the side of the triangles in the coarse gird. The grid does not change as inclusion separation changes. The thickness deformation at node i is denoted by u_i.

Using methods similar to those in ref. 29 and 30 the energy is first written in a discrete form and then the thickness deformation field that minimizes this energy is computed. Finally, the minimizer is plugged back into the energy expression. Thus, the problem to be solved is

$$\begin{aligned}\phi &= \min_{u_i} K_b V_i \sum_i \left(\sum_{c=1}^{6} u_i^c - 6u_i\right)^2 \frac{2}{9\ell^4} + \sum_i \frac{V_i}{2} K_t \left(\frac{u_i}{a}\right)^2 \\ &\quad + \sum_i \frac{F u_i V_i}{a} + \sum_{i,j,k} \frac{F A_{ijk}}{3\ell^2}\left[(u_i-u_j)^2 + (u_j-u_k)^2 + (u_k-u_i)^2\right] \\ &= \min_{\mathbf{u}} \mathbf{u}^T \mathbf{M} \mathbf{u} + \lambda \mathbf{u}^T \mathbf{1}_\mathbf{u}.\end{aligned} \tag{14}$$

For nodes i in the coarse or fine grid that are far away from the interface or the boundary of an inclusion (for example, see the purple node in Fig. 4(c)) $u_i^c, c = 1, 2, \ldots, 6$ are the thickness deformations at the nodes surrounding node i. In the above V_i is the area of the Voronoi cell around node i and l is the side of the triangle. When node i is located at the boundary of an inclusion then the appropriate V_i is shown around the white node in Fig. 4(c) and the sum over c in the first term is computed by assuming that the inclusion is flat. When node i is at the interface between the fine and coarse grid (see the yellow node in Fig. 4(c)) then the appropriate V_i is shown around the yellow node in Fig. 4(c) and we have to use different weights depending on where u_i^c is in the coarse grid or the fine grid.§ In the final discrete version of the energy expression, $\mathbf{1}_\mathbf{u}$ is a column vector of size len($\mathbf{u}$) with all entries 1 and $\lambda = \frac{FV_i}{a}$. M is the stiffness matrix where M_{ij} multiplies $u_i u_j$. It has been shown[8] that the boundary condition can be written in the discrete form,

$$u(r_i, \theta_i) = U(\theta_i), \forall i \text{ on the boundary} \tag{15}$$

$$\frac{u_k - \frac{1}{2}(u_i + u_j)}{\sqrt{3}\ell/2} = U'(\theta_{i'}), \forall i', i, j, k \text{ pairs along the boundary}$$

(i' is the midpoint of i and j, see Fig. 4(a)). (16)

Note that u_i, u_j are given in eqn (15) and thus u_k can be solved from eqn (16) immediately. We also assume that the inclusions are flat. Hence, eqn (14) can be rewritten as,

$$\begin{aligned}\phi &= \min_{\mathbf{u_a}} \begin{bmatrix}\mathbf{u_a}\\ \mathbf{u_b}\end{bmatrix}^T \begin{bmatrix}\mathbf{M_{aa}} & \mathbf{M_{ab}}\\ \mathbf{M_{ab}^T} & \mathbf{M_{bb}}\end{bmatrix} \begin{bmatrix}\mathbf{u_a}\\ \mathbf{u_b}\end{bmatrix} + \lambda \begin{bmatrix}\mathbf{u_a}\\ \mathbf{u_b}\end{bmatrix}^T \begin{bmatrix}\mathbf{1_a}\\ \mathbf{1_b}\end{bmatrix} \\ &= \mathbf{u_a^T M_{aa} u_a} + 2\mathbf{u_a^T M_{ab} u_b} + \mathbf{u_b^T M_{bb} u_b} + \lambda \mathbf{u_a^T 1_a} + \lambda \mathbf{u_b^T 1_b}.\end{aligned} \tag{17}$$

In the above $\mathbf{u_b}$ is the vector of all nodes determined by eqn (15) and (16) and $\mathbf{u_a}$ is the vector of all nodes that are not in $\mathbf{u_b}$. Taking $\frac{\partial(\mathbf{u^T M u} + \lambda \mathbf{u^T 1_u})}{\partial \mathbf{u_a}} = 0$, we get $\bar{\mathbf{u}}_\mathbf{a} = -\mathbf{M_{aa}}^{-1}\left(\mathbf{M_{ab} u_b} + \frac{\lambda}{2}\mathbf{1_a}\right)$ at which eqn (17) is minimized where $\mathbf{1_a}$ is a column vector of size len($\mathbf{u_a}$) with all entries 1. Then, we can write the minimized total energy as,

$$\begin{aligned}\phi &= \left(\frac{\lambda}{2}\mathbf{1_a^T} + \mathbf{u_b^T M_{ab}^T}\right)\mathbf{M_{aa}}^{-1}\left(\mathbf{M_{ab} u_b} + \frac{\lambda}{2}\mathbf{1_a}\right) - 2\left(\frac{\lambda}{2}\mathbf{1_a^T} + \mathbf{u_b^T M_{ab}^T}\right) \\ &\quad \times \mathbf{M_{aa}}^{-1}\mathbf{M_{ab} u_b} + \mathbf{u_b^T M_{bb} u_b} - \lambda\left(\frac{\lambda}{2}\mathbf{1_a^T} + \mathbf{u_b^T M_{ab}^T}\right)\mathbf{M_{aa}}^{-1}\mathbf{1_a} \\ &\quad + \lambda \mathbf{u_b^T 1_b}.\end{aligned} \tag{18}$$

In Fig. 3(b) we compare the numerical solution of eqn (2) for the thickness deformation profile around one hexagon shaped inclusion using the above finite difference technique with the analytical solution eqn (4) with $N = 8$, $K_b = 20\ k_B T$, $K_t = 60\ k_B T\ nm^{-2}$, $F = 1$ pN nm^{-1}, boundary conditions $U_1 = -0.5$ nm, $U_1' = 0$ where k_B is the Boltzmann constant and $T = 300$ K is the absolute temperature and find excellent agreement as n increases. Unless indicated otherwise, we use these parameter values in all calculations in this work. This shows that the analytical and numerical methods to compute the thickness deformation profiles are consistent with each other and with the results of molecular simulations documented in the literature. We use $n = 20$ in all the energy computations henceforth for each of the three different types of inclusions studied.

2.3 Applications to hexagon, rod and star shaped inclusions

We now focus on the interaction of two hexagon shaped inclusions on a lipid membrane which has a rotational periodicity of $\pi/3$. We use eqn (18) derived from our numerical method and eqn (12) derived from the analytical method, to compute the interaction energy of two inclusions separated by distance r and then make comparisons. As shown in Fig. 5(a), the energy computed using the analytical method for two inclusions separated by distance r in two different orientations (shown in the inset differing by a rotation of $\pi/6$) are almost the same. Hence, we can simplify our model and consider the energy landscape generated by two hexagon inclusions as being almost isotropic (insensitive to rotation). In Fig. 5(b), we fix the shape of the two hexagons (see inset of the figure), and show that as n increases, the match between the energy computed from the numerical method and analytical method gets better, justifying our numerical approach of using a fine grid when the inclusions are nearby. From Fig. 5(c) we learn that as applied tension increases, the attraction at small separations (around

§ Slightly different weights for computing the energy contributions of the interface nodes do not change the final result for the profiles of u or the minimized energy.

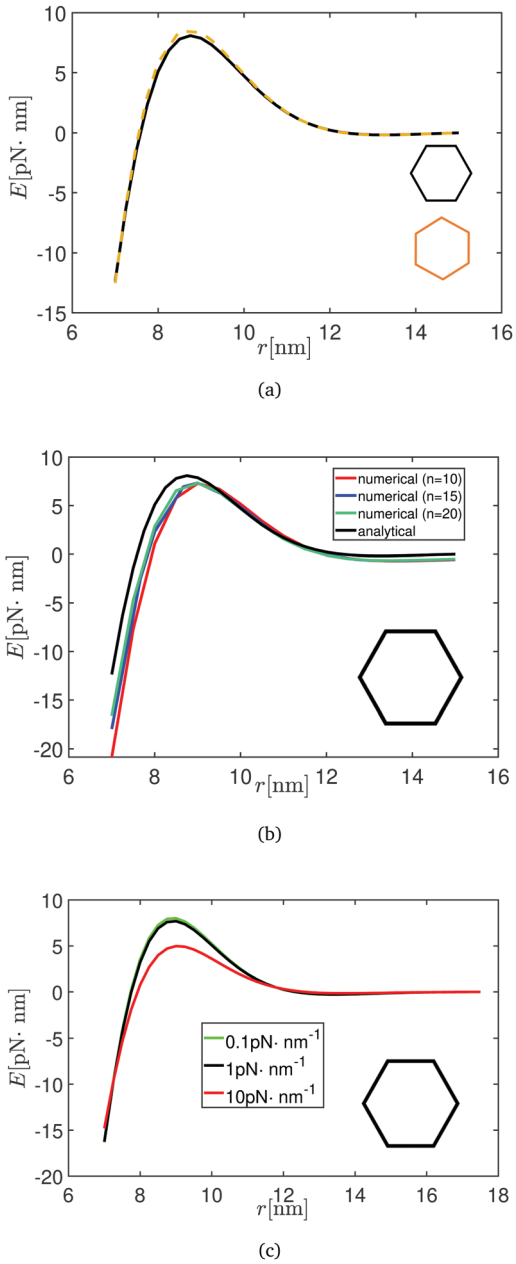

Fig. 5 (a) The energy computed by the analytical method using eqn (12) for two configurations of hexagon inclusions differing by a rotation of $\pi/6$ under F = 1 pN nm^{-1}. (b) The energy of the configuration with F = 1 pN nm^{-1} computed numerically using eqn (18) converged to the energy computed by eqn (12) as n increases. Recall that the side of the triangles in the fine grid is $1/n$ that of the coarse grid. (c) A comparison of the energy profiles at three different applied tensions: 0.1 pN nm^{-1}, 1 pN nm^{-1}, 10 pN nm^{-1}.

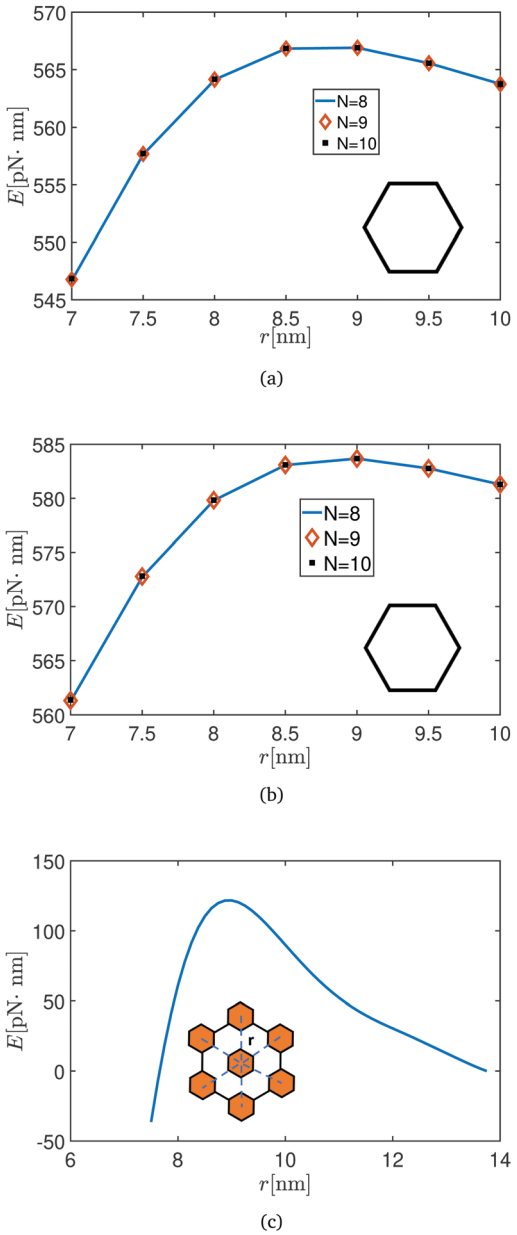

Fig. 6 The energy computed using different number of terms in the series (N = 8,9,10) in eqn (4) under applied tension (a) 1 pN nm^{-1}, (b) 10 pN nm^{-1}. The energy computed with different N are almost identical. For this reason we use N = 8 in eqn (4) for all energy computations. The energy in these two plots is not scaled by subtracting the value at $r = R_2$. (c) The energy of a cluster of seven hexagons (one fixed at the center) as a function of separations r under applied tension F = 1 pN nm^{-1}. There is a maximum around r = 9 nm which is similar to the findings in ref. 29 that focuses on bending deformations and those in ref. 6 that analyzes thickness deformations.

$r = R_1$ = 7 nm) becomes weaker, but the repulsive force at around 9–10 nm also becomes weaker. In Fig. 5 we study short range interactions as small as center-to-center distance 7 nm for two hexagon inclusions. The side of the hexagon is 2.5 nm, so a 7 nm center-to-center distance corresponds to about 2 nm distance between their boundaries, which corresponds to two lipid molecules. At such small separations we do not expect that minimization of the continuum expression eqn (1) will capture molecular level deformations, although it has been shown previously that it captures many aspects of protein-induced bilayer perturbations.[6,31,32] For this reason, in later computations of the first passage time we take R_1 = 9 nm for both hexagon and star inclusions. Fig. 6(a) and (b) show that the computed energy hardly changes as we increase N from N = 8 to

N = 9, 10 in eqn (12). For this reason we use N = 8 for all the computations in this work. In Fig. 6(c), we compute the energy due to thickness deformations of a cluster of seven inclusions as shown in the inset using our finite difference method. We find a maximum in the energy around r = 9 nm similar to the findings in ref. 27 and 29 which studied interactions of inclusions due to membrane bending deformations in the presence of fluctuations and those in ref. 6 which studied thickness deformations of MscL lattice. We do not assume pairwise additivity of the energy in any of our computations (including those with 7 inclusions) because the thickness deformation field is solved by minimizing eqn (1) with boundary conditions applied at each inclusion.

Fig. 7(a) shows that the energy landscape of two rod shaped inclusions is anisotropic – at small separations the force is repulsive at $\theta = 0^\circ$ and becomes attractive at some angle around $40^\circ < \theta < 50^\circ$. The attraction increases as θ goes up to 90°. This behavior of the energy of two rod shaped inclusions is reminiscent of the energy from out-of-plane deflection for two rods[27] on a lipid membrane. Fig. 7(b) shows that the energy computed by the numerical method and analytical method again agree very well which gives us confidence in the numerical method.

Next we compute the interaction energy of rod shaped inclusions for tensions F = 0.1 pN nm^{-1} and F = 10 pN nm^{-1}. The comparison between Fig. 8 and 7(a) shows that as applied tension increases, the interaction force becomes weaker at short separations, which implies that elastic interactions could be weakened by strong applied tension. Physically, this is reasonable, since high tension will tend to make the membrane flatter so that the thickness is more uniform everywhere.

Next, we apply both methods to compute the interaction energy of two star shaped inclusions in Fig. 9. Just as in the case of hexagons, we consider various orientations of the star shaped inclusions as shown in the inset of Fig. 9(a). The match between the analytical method and numerical method is not as good in this case because the star shaped inclusion has 12 vertices at which the derivative along normal directions are discontinuous. Since in the analytical method we used Fourier–Bessel series to approximate the contour $(\mathscr{R}_1,\mathscr{R}_2)$ and the derivative along normal directions to the boundaries, it requires a large number of terms N to obtain a good approximation. This is computationally not feasible for symbolic operations in MATLAB. Thus, we have greater confidence in our finite difference numerical method to compute interaction energies in complex geometries. In Fig. 9(b) we use our numerical method to compute the interaction energies for star shaped inclusions for various values of F. The trends are similar to those

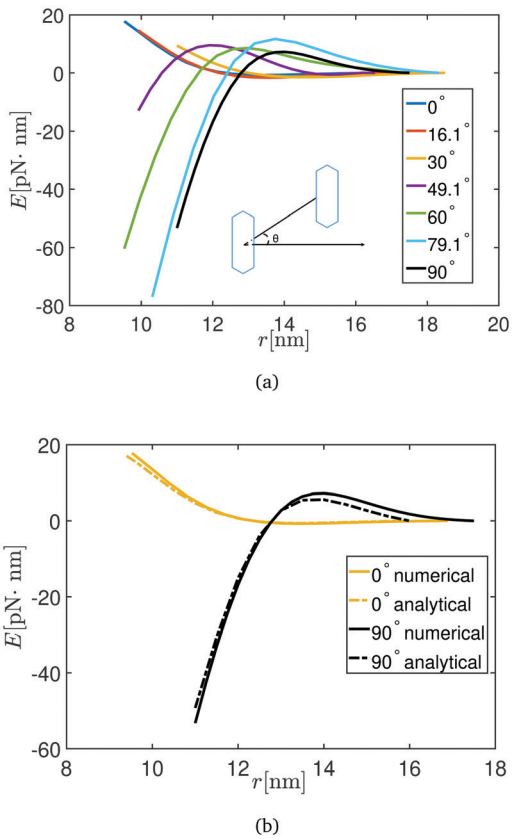

Fig. 7 (a) The energy of two rod shaped inclusions computed by numerical method eqn (18) with different θ under applied tension 1 pN nm^{-1}. (b) The energy computed by analytical method using eqn (12) fits the one computed by numerical method using eqn (18) both with $\theta = 0^\circ$ and $\theta = 90^\circ$ under applied tension 1 pN nm^{-1}.

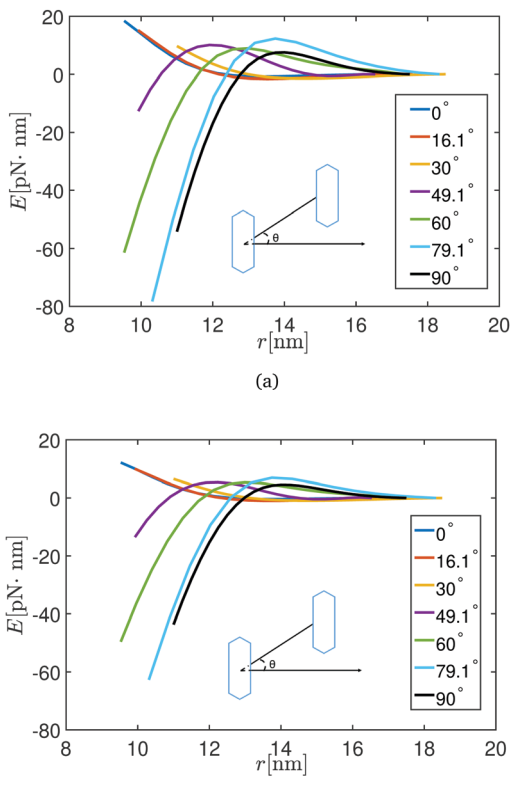

Fig. 8 (a) The energy of two rod shaped inclusions computed by numerical method eqn (18) with different θ under applied tension 0.1 pN nm^{-1}. (b) The energy of two rod shaped inclusions computed by numerical method eqn (18) with different θ under applied tension 10 pN nm^{-1}.

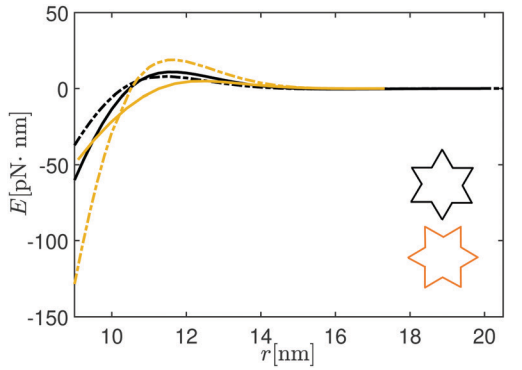

(a)

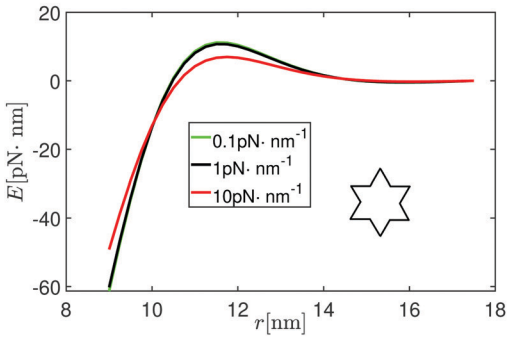

(b)

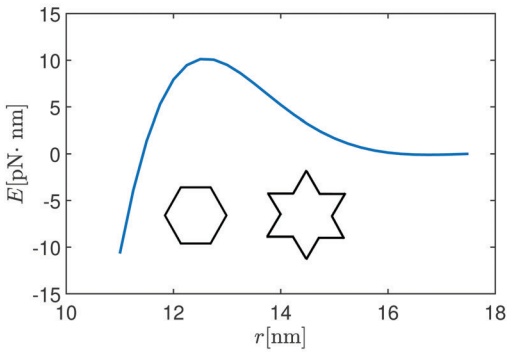

(c)

Fig. 9 (a) Solid lines are the energy of two star inclusions with different rotational angles computed by numerical method using eqn (18) and dashed lines are the energy computed by analytical method using eqn (12). The applied tension is 1 pN nm^{-1}. (b) The energy of two star inclusions computed by numerical method under three applied tensions: 0.1 pN nm^{-1}, 1 pN nm^{-1}, 10 pN nm^{-1}. (c) The energy of one hexagon inclusion and one star inclusion under applied tension 1 pN nm^{-1}.

seen for hexagon shaped inclusions. Finally, in Fig. 9(c) we compute the energy of one hexagon and one star inclusion separated by distance r and find again that there is a maximum in the curve around r = 12 nm.

This completes our analysis of the interaction energy of inclusions due to bilayer thickness interactions. In most cases we have shown that there is a maximum in the interaction energy of two inclusions around a separation r = 10 nm. For separations smaller than this value there is a strong attractive force between the inclusions which will cause them to coalesce. In the next section we will compute the time to coalescence as a function of the initial separation between the inclusions.

3 First passage time for isotropic inclusions under mixed boundary condition

Our main goal in this paper is to study the kinetics of an inclusion diffusing in an energy landscape resulting from elastic interactions with another inclusion. Efficient methods to compute the energy landscape developed above are a pre-requisite to this exercise. We will now use these methods to solve first passage time problems.

We consider a circular membrane of size R_2 = 125 nm with a circular inclusion of size 2.5 nm fixed at the center. Another circular inclusion of the same size is diffusing around driven by stochastic forces. Recall from the energy landscape that there are attractive interactions between inclusions when the separations are small. Hence, if the moving inclusion comes close enough to the static one at the center then it will be strongly attracted. Therefore, we assume that at R_1 = 7 nm there is an absorbing wall at which the moving inclusion will disappear by being attracted towards the center. We assume that at R_2 = 125 nm (far away) there is a reflecting wall where the moving inclusion will be bounced back. Note that problems in which both boundaries are absorbing were solved elsewhere.[27] The exercise we will perform now is as follows. We place the second inclusion randomly on a circle of radius $r = y$ at time t = 0 and let it diffuse around. At some time $t = T_{\text{in}}$ when the inclusion hits the inner boundary for the first time we stop it from diffusing and record T_{in}. We repeat this experiment a large number of times and record T_{in} for each repetition. The mean value of T_{in} is the mean first passage time T_1. Our goal is to find $T_1(y)$ as a function of the initial condition $r = y$. This can be done analytically or through a Langevin dynamics simulation. We will use both methods in the following.

To estimate $T_1(y)$ analytically we first need to compute survival probabilities. Let p be the probability density (for finding the inclusion) at position r and angle θ given initial condition $r = y$, $\theta = \alpha$ and $P(r,t|y) = \int_0^{2\pi} p(r,t,\theta|y,\alpha)\mathrm{d}\theta$. The probability density p is independent of θ since neither the energy landscape nor the diffusion (or drag) coefficient of the inclusion depends on it. As a result, the Fokker–Planck equation for the evolution of this probability is in the following isotropic form,[27]

$$\frac{\partial P}{\partial t} = \frac{\partial}{\partial r}\left[\frac{1}{\nu}\frac{\partial \phi}{\partial r}P + D\frac{\partial P}{\partial r}\right] + \frac{1}{r}\left[\frac{1}{\nu}\frac{\partial \phi}{\partial r}P + D\frac{\partial P}{\partial r}\right], \tag{19}$$

with Dirichlet boundary condition at the inner boundary and Robin boundary condition at the outer boundary,[33]

$$P(R_1,t) = 0, \quad \left(k_{\text{B}}\text{T}\frac{\partial P}{\partial r} + \frac{\partial \phi}{\partial r}P\right)\Big|_{(R_2,t)} = 0, \quad \forall t \geq 0. \tag{20}$$

The first equation in eqn (20) is an absorbing boundary condition at R_1 which means that if the moving particle hits this wall it is absorbed and exits the kinetics. So, the probability to find such a particle at the absorbing wall is zero. The second equation in eqn (20) is the reflecting boundary condition at R_2. It means that when the moving particle hits the reflecting wall it will bounce back, hence the probability current at this point will be zero.[33] In the above D is a diffusion coefficient of the inclusion in the lipid membrane and ν is a drag coefficient which are related by the Nernst–Einstein relation $\nu D = k_B T$.[27] Let $S(y,t)$ be the survival probability,

$$S(y,t) = \int_{R_1}^{R_2} P(r,t|y) r \mathrm{d}r. \tag{21}$$

Then, we can get the first passage time density,

$$f(y,t) = -\frac{\partial S(y,t)}{\partial t} = -\int_{R_1}^{R_2} \frac{\partial P(r,t|y)}{\partial t} r \mathrm{d}r. \tag{22}$$

The existence of the first moment of $P(r,t|y)$ with respect to time t can be shown from the fundamental solution constructed by Itô in ref. 34. Then, $tP(r,t|y) \to 0$ as $t \to \infty$. Accordingly, the first passage time $T_1(y)$ can be derived from eqn (22),

$$\begin{aligned} T_1(y) &= \int_0^\infty f(y,t) t \mathrm{d}t = -\int_0^\infty \int_{R_1}^{R_2} \frac{\partial P(r,t|y)}{\partial t} r \mathrm{d}r t \mathrm{d}t \\ &= \int_{R_1}^{R_2} \int_0^\infty P(r,t|y) \mathrm{d}t r \mathrm{d}r = \int_{R_1}^{R_2} g_1(r,y) r \mathrm{d}r, \end{aligned} \tag{23}$$

where g_1 is defined by,

$$g_1(r,y) = \int_0^\infty P(r,t|y) \mathrm{d}t. \tag{24}$$

Theorem 1: the ODE for $T_1(y)$ with a reflecting wall at the outer boundary and an absorbing wall at the inner boundary is

$$\frac{\partial^2 T_1(y)}{\partial y^2} + \left(-\frac{1}{k_B T} \frac{\partial \phi}{\partial y} + \frac{1}{y} \right) \frac{\partial T_1(y)}{\partial y} + \frac{1}{D} = 0, \tag{25}$$

with boundary conditions,

$$T_1(R_1) = 0, \quad T_1'(R_2) = 0. \tag{26}$$

Proof: see proof of Theorem 1.

Next, we describe how to estimate $T_1(y)$ using Langevin dynamics simulations. The overdamped version of the Langevin equation in an isotropic setting is given by,[27]

$$\mathrm{d}r_i = -\frac{1}{\nu} \frac{\partial \phi}{\partial r_i} \mathrm{d}t + \sqrt{\frac{2 k_B T \mathrm{d}t}{\nu}} \xi_i, \tag{27}$$

where i represents two perpendicular directions of the motion. ν is the translational drag coefficient of a circular inclusion which is calculated using the Saffman–Delbrck model,

$$\nu = \frac{4\pi\eta_m}{\log(2\varepsilon^{-1}) - \gamma}, \tag{28}$$

where $\eta_m = 15.3 \times 10^{-9}$ Pa s m is the membrane viscosity (2D), $\eta_w = 8.5 \times 10^{-4}$ Pa s is the bulk viscosity of water (3D), $\ell = 2.5$ nm is the radius of the circular cross section of the inclusion, $\varepsilon = 2\eta_w \ell / \eta_m$ and $\gamma \approx 0.577$ is Euler's constant.[35] Then we use the Einstein relation $D = k_B T/\nu$ to compute the diffusion coefficient D. For more details we refer the readers to ref. 27. The drag and diffusion coefficient are

Table 1 List of parameters

Symbol	Description	Units	Typical values
ℓ	Side length of triangular grid	nm	2.5
K_b	Bending modulus	pN nm	82.8[6]
T	Temperature	K	300
k_B	Boltzmann constant	N m K^{-1}	1.38×10^{-23}
K_t	Thickness deformation modulus	pN nm^{-1}	248.4[6]
r	Separations between two inclusions	nm	9–125
F	Applied tension	pN nm^{-1}	0.1–10
a	Unperturbed bilayer half-thickness	nm	1.75[11]
$\mathscr{R}_1(\theta_1)$	Shape function for the centered inclusion	nm	
$\mathscr{R}_2(\theta_2)$	Shape function for the moving inclusion	nm	
θ	The angle between two inclusions and horizontal line (see Fig. 2(b))	radian per degree	
u	Thickness deformation	nm	
u_i	Thickness deformation at node i	nm	
V_i	The area of the Voronoi cell at node i	nm^2	
A_{ijk}	The area of the triangle with vertices i,j,k	nm^2	
R_1	Radius of the inner boundary for diffusing inclusion	nm	
R_2	Radius of the outer boundary for diffusing inclusion	nm	
$\mathbf{u_b}$	The vector of all nodes determined by eqn (15) and (16)		
$\mathbf{u_a}$	The vector of all nodes that are not in $\mathbf{u_b}$		
$\mathbf{u}$	$\mathbf{u} = [\mathbf{u_a}^T, \mathbf{u_b}^T]^T$		
ϕ	Energy of the system	pN nm	
n	Ratio of side of triangle in the coarse grid to that in the fine grid		
$\nu(\nu_{ij})$	Translational drag coefficient (tensor for anisotropic inclusion)	s pN nm^{-1}	2.32×10^{-5} [27]
$D(D_{ij})$	Diffusion coefficient (tensor for anisotropic inclusion)	nm^2 s^{-1}	1.76×10^{5} [27]
T_n	Chebyshev polynomials of the first kind		
U_n	Chebyshev polynomials of the second kind		
K_n	Modified Bessel functions of the second kind		

both given in Table 1. We have neglected rotational diffusion here because it is shown in ref. 27 that it does not play a major role in determining the first passage time. $\xi_i \sim \mathcal{N}(0,1)$, a normally distributed random variable with mean 0 and variance 1, represents the stochastic force along direction i. We initially put the moving particle somewhere at $r = y$, and choose a time step dt that ensures convergence of the Lagenvin dynamics simulation. Then, for each time step dt, we perform the calculation in eqn (27), updating the position of the moving inclusion. We record the time at which the moving particle hits the absorbing wall at R_1. We run 8000 simulations and then take an average to estimate the first passage time. For more details the readers are referred to ref. 27. Fig. 5(a) and 9(a) show that the $\phi(\mathbf{r})$ for hexagon and star inclusions can be regarded as nearly isotropic. For these we use eqn (25) to numerically solve for the first passage time and compare it with the results obtained from the Langevin simulations. Since inclusions have non-zero size and our computations of the interaction energy $\phi(\mathbf{r})$ are not meaningful if the distance between their boundaries (not centers) is comparable to the size of a lipid headgroup (which is 1 nm), so we choose $R_1 = 9$ nm for isotropic inclusions (hexagon, star) and $R_1 = 11$ nm for anistropic inclusion (rod) in our first passage time calculations.

Fig. 10 shows that the first passage time for hexagonal inclusion derived from the two methods are in good agreement. As the applied tension increases, the first passage time is reduced at most r that are not close to R_1. At first glance this might seem counter-intuitive because from Fig. 5(c) we know that at small separations (close to R_1) the attraction force

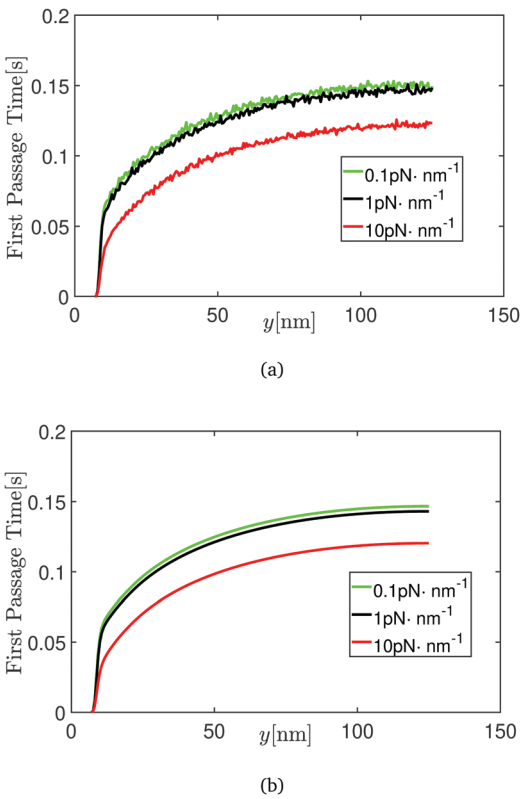

Fig. 10 The first passage time for two hexagon inclusions is computed using (a) Langevin dynamics simulations in eqn (27), (b) ODE in eqn (25) under three applied tensions 0.1 pN nm^{-1}, 1 pN nm^{-1}, 10 pN nm^{-1}.

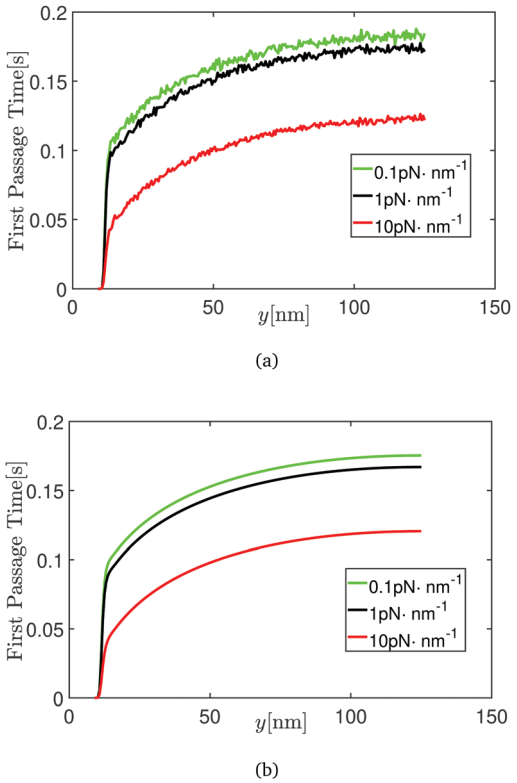

Fig. 11 The first passage time for two star inclusions is computed by (a) Langevin dynamics simulations in eqn (27), (b) ODE in eqn (25) under three applied tensions 0.1 pN nm^{-1}, 1 pN nm^{-1}, 10 pN nm^{-1}.

becomes weaker as applied tension increases. However, there is a stronger repulsive force at around r = 9–10 nm under small applied tension which slows the motion of the moving particle from a large starting separation (see Fig. 5(c)).

The first passage time computed by the two methods is also in good agreement when the inclusions are star shaped (see Fig. 11). The order of the first passage time is the same as the hexagonal inclusions and similar arguments for the shape of the curves can be made here.

The first passage times in all the above computations are dominated by the Brownian motion because the membrane thickness mediated interactions play a significant role only for small separations y. To validate our methods for stronger and longer range interactions between inclusions we choose $\phi = \frac{50}{r}$ to mimic electrostatic interactions between point charges and use eqn (27) and (25) to compute the first passage times. The time step used in all previous Langevin simulations is dt = 10^{-6} s. However, we did a small number of Langevin simulations with dt = 10^{-7} to validate our results. From Fig. 12 we see that as dt decreases to 10^{-7} in eqn (27) the first passage time computed by Langevin simulations (green curves) converges to the one solved from the ODE in eqn (25). The purple curve in Fig. 12 is derived by setting $\phi = 0$ in eqn (27) and eqn (25) for the purpose of comparison. It is clear that the repulsive electrostatic force slows down the kinetics of coalescence of the moving particle. These results show that our methods are also applicable in scenarios where deterministic forces play an important role in the interactions of the inclusions.

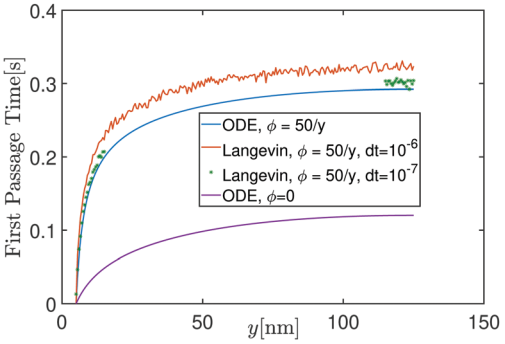

Fig. 12 The first passage time for hexagon inclusions with electrostatic potential $\phi = \frac{50}{r}$ estimated by Langevin equation eqn (27) with time step $dt = 10^{-6}$ (orange), with time step $dt = 10^{-7}$ (green), by ODE eqn (25) (blue) under applied tension 1 pN nm^{-1}. The purple curve is solved from eqn (25) by setting $\phi = 0$ as a comparison.

4 First passage time for anisotropic inclusions under mixed boundary condition

For two non-circular inclusions, the corresponding Fokker–Planck equation for the probability density p is a partial differential equation of parabolic type,[27]

$$\begin{aligned}\frac{\partial p}{\partial t} &= \frac{\partial}{\partial x_i}\left[\nu_{ij}^{-1}\frac{\partial \phi}{\partial x_j}p\right] + \frac{\partial^2}{\partial x_i \partial x_j}[D_{ij}p] \\ &= \frac{1}{\nu_a}\left(\frac{\partial^2 \phi}{\partial {x_1}^2}p + \frac{\partial \phi}{\partial x_1}\frac{\partial p}{\partial x_1}\right) + \frac{1}{\nu_b}\left(\frac{\partial^2 \phi}{\partial {x_2}^2}p + \frac{\partial \phi}{\partial x_2}\frac{\partial p}{\partial x_2}\right) \\ &\quad + D_a\frac{\partial^2 p}{\partial {x_1}^2} + D_b\frac{\partial^2 p}{\partial {x_2}^2}.\end{aligned} \tag{29}$$

Accordingly, we need to redefine the first passage time in eqn (23) which is now given by,

$$\begin{aligned}T_1(y,\alpha) &= \int_0^\infty f(y,\alpha,t)t\mathrm{d}t = -\int_0^\infty \int_{R_1}^{R_2}\int_0^{2\pi}\frac{\partial p(r,\theta,t|y,\alpha)}{\partial t}r\mathrm{d}r\mathrm{d}\theta t\mathrm{d}t \\ &= \int_{R_1}^{R_2}\int_0^{2\pi}\int_0^\infty p(r,\theta,t|y,\alpha)\mathrm{d}t\mathrm{d}\theta r\mathrm{d}r \\ &= \int_{R_1}^{R_2}\int_0^{2\pi} q_1(r,\theta|y,\alpha)\mathrm{d}\theta r\mathrm{d}r,\end{aligned} \tag{30}$$

where $tp(r,\theta,t|y,\alpha) \to 0$ as $t \to \infty$ is implemented in the first equation of the second line and q_1 is defined by,

$$q_1(r,\theta|y,\alpha) = \int_0^\infty p(r,\theta,t|y,\alpha)\mathrm{d}t. \tag{31}$$

Theorem 2: the PDE for $T_1(y,\alpha)$ with a reflecting wall at the outer boundary and an absorbing wall at the inner boundary is given below,

$$\begin{aligned}&\left(D_a\cos^2\alpha + D_b\sin^2\alpha\right)\frac{\partial^2 T_1}{\partial y^2} + \left(D_a\frac{\sin^2\alpha}{y^2} + D_b\frac{\cos^2\alpha}{y^2}\right)\frac{\partial^2 T_1}{\partial \alpha^2} \\ &+ \left(-D_a\frac{\sin 2\alpha}{y} + D_b\frac{\sin 2\alpha}{y}\right)\frac{\partial^2 T_1}{\partial y \partial \alpha} + \left[D_a\frac{\sin^2\alpha}{y} + D_b\frac{\cos^2\alpha}{y}\right. \\ &\left. + \frac{1}{\nu_a}\left(\frac{\sin 2\alpha\frac{\partial \phi}{\partial \alpha}}{2y} - \cos^2\alpha\frac{\partial \phi}{\partial y}\right) - \frac{1}{\nu_b}\left(\frac{\sin 2\alpha\frac{\partial \phi}{\partial \alpha}}{2y} + \sin^2\alpha\frac{\partial \phi}{\partial y}\right)\right]\frac{\partial T_1}{\partial y} \\ &+ \left[D_a\frac{\sin 2\alpha}{y^2} - D_b\frac{\sin 2\alpha}{y^2} + \frac{1}{\nu_a}\left(\frac{\sin 2\alpha\frac{\partial \phi}{\partial y}}{2y} - \frac{\sin^2\alpha\frac{\partial \phi}{\partial \alpha}}{y^2}\right)\right. \\ &\left. - \frac{1}{\nu_b}\left(\frac{\sin 2\alpha\frac{\partial \phi}{\partial y}}{2y} + \frac{\cos^2\alpha\frac{\partial \phi}{\partial \alpha}}{y^2}\right)\right]\frac{\partial T_1}{\partial \alpha} + 1 = 0,\end{aligned} \tag{32}$$

with boundary conditions

$$T_1(R_1,\alpha) = 0, \frac{\partial T_1}{\partial y}(R_2,\alpha) = 0, T_1(y,0) = T_1(y,2\pi). \tag{33}$$

Proof: see proof of Theorem 2.

The overdamped Langevin equation in an anisotropic setting is given by,[27]

$$\mathrm{d}r_i = -\nu_{ij}^{-1}\frac{\partial \phi}{\partial r_j}\mathrm{d}t + \sqrt{\frac{2k_BT\mathrm{d}t}{\nu_{ii}}}\xi_i(\text{no sum in the second term}), \tag{34}$$

where i represents two perpendicular directions of the motion and ν_{ij} and ξ_i are the drag coefficient tensor and random force tensor. Note that for a rod shaped inclusion the drag coefficient along the longitudinal direction is smaller than that perpendicular to it. The details for how to compute these drag coefficients can be found in ref. 27. Fig. 7(a) shows that the interaction energy $\phi(\mathbf{r})$ for rod shaped inclusions depends on θ (it is anisotropic). In the Langevin dynamics calculations, for each initial position y we use eqn (34) to run 8000 simulations with a reflecting wall at R_2 and an absorbing wall at R_1 for four $\theta = 0^\circ, 30^\circ, 60^\circ, 90^\circ$ and then take an average (for each θ separately) to estimate the first passage time. We also use eqn (32) to numerically solve the first passage time and compare the results derived from the two methods for $F =$ 0.1,1,10 pN nm^{-1} in Fig. 13–15, respectively.

The good agreement between the first passage time solved from the PDE in eqn (32) and estimated by Langevin equation once again shows that our methods work well. As shown in Fig. 13, as the initial angle increases from 0° to 90°, the first passage time decreases at small separations, but increases at large separations. This can be explained by the fact that stronger attractive force near R_1 pulls the moving particle to be absorbed faster from smaller initial separations while stronger repulsive force around 12–16 nm leads to a larger first passage time when the particle is initially located at a large distance.

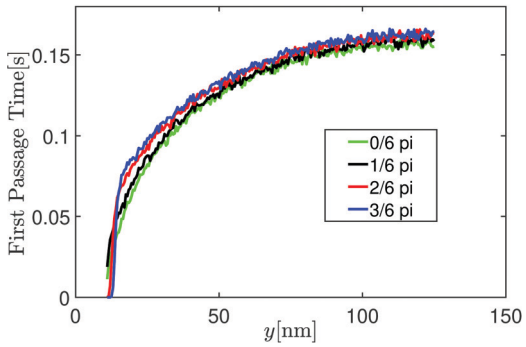

(a)

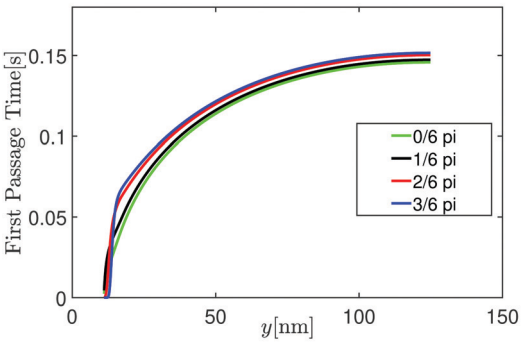

(b)

Fig. 13 The first passage time for two rod inclusions computed from (a) Langevin dynamics using eqn (34), (b) PDE using eqn (32) under applied tension 0.1 pN nm^{-1}.

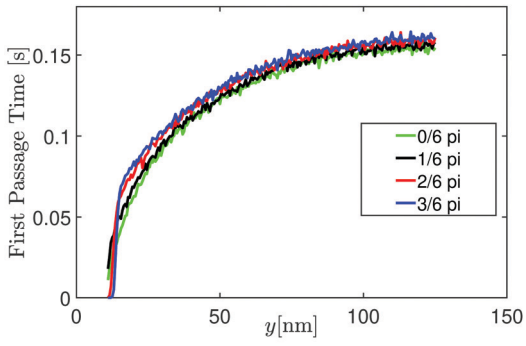

(a)

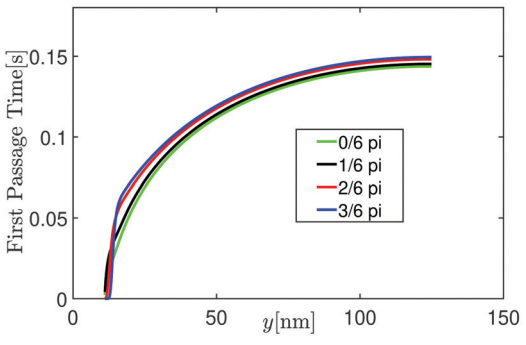

(b)

Fig. 14 The first passage time for two rod inclusions computed from (a) Langevin dynamics using eqn (34), (b) PDE using eqn (32) under applied tension 1 pN nm^{-1}.

The result of the first passage time under 1 pN nm^{-1} applied tension in Fig. 14 is similar to the one under 0.1 pN nm^{-1} applied tension.

Compared to the results under 0.1,1 pN nm^{-1} applied tension, the first passage time is reduced under 10 pN nm^{-1} applied tension. The order of magnitude of the first passage time under all three tensions is similar.

5 Discussion

This paper has two major parts. In the first part we use a finite difference method to compute the interaction energy of two inclusions due to membrane thickness deformations. In the second part we use the computed energy landscape to solve first passage time problems. Our method to compute energies is different from the analytical method in ref. 7 and 8 which uses perturbation theory to study thickness mediated interactions between two anisotropic inclusions; we implement an approach to compute the energy using the divergence theorem which is more general and can deal with strongly anisotropic inclusions. The advantage of analytical methods in both ref. 7 and 8 and this work is that they can compute the energy accurately at small applied tension F if enough terms in the Fourier–Bessel series are used. However, it is time consuming to compute the coefficients in the Fourier–Bessel series and this becomes computationally infeasible when the inclusions are strongly anisotropic. On the other hand, our numerical method is able to handle arbitrary values of F and can efficiently compute the interaction energy of two inclusions for different separations $\mathbf{r}$ given a fixed set of parameters (K_b,K_t,*a etc.*) which are stored in a pre-calculated stiffness matrix.

In the second part of the paper we compute the time to coalescence of two inclusions of various shapes as a function of the distance separating them. We use both Langevin dynamics and a PDE to arrive at our estimates. For two inclusions separated by about 125 nm we predict that the time to coalescence is hundreds of milliseconds irrespective of the shape of the inclusion. The time to coalescence with only membrane bending interactions was of similar magnitude as shown in ref. 27. The order of magnitude of the time to coalescence is the same even though the attractive force due to membrane thickness interactions is stronger than that due to membrane bending interactions in ref. 27 at small separations. The reason is that even with membrane thickness interactions the attractive force decays to zero quickly and Brownian motion dominates the kinetics of the moving particle in most regions, just as in ref. 27. Therefore, at small separations the first passage time with thickness mediated interactions is smaller than that with out-of-plane bending interactions, but is not very different at large separations. The time to coalescence at large separations can be changed from that dictated by Brownian motion alone if longer range interactions (for instance, due to electrostatics) are taken into account as shown in Fig. 12.

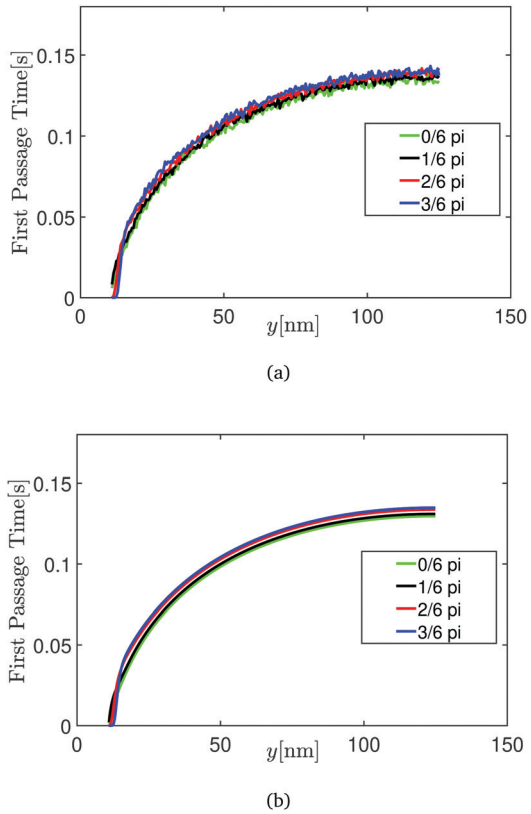

Fig. 15 The first passage time for two rod inclusions computed from (a) Langevin dynamics using eqn (34), (b) PDE using eqn (32) under applied tension 10 pN nm^{-1}.

6 Conclusion

In this paper we have analyzed the temporal self-assembly of inclusions due to interactions mediated by membrane thickness variations. It is shown that the results from Langevin dynamics simulations agree well with those obtained from a PDE for the first passage time. The approach based on the PDE is much faster than the Langevin dynamics simulation and could open new ways to study the process of self-assembly. This is a step beyond earlier studies which focused on the energy landscape of clusters of proteins, but did not look into kinetics. Some papers based on molecular simulation did consider the temporal process, but to the best of our knowledge most did not reach the time scales calculated in this paper. Phase-field methods can compute the evolution of particle concentrations on a membrane, but it is beyond their scope to track the motion of discrete particles as we have done here. We close this paper by mentioning some effects that we did not consider. First, hydrodynamic interactions between inclusions (based on the Oseen tensor) were shown to speed up self-assembly in ref. 27 and they are expected to have a similar effect here. Second, the temporal behavior of a cluster of inclusions are not studied in this paper due to limitations of computational power, but we expect the overall behavior to be similar to the clusters studied in our earlier work.[27] Third, only a limited set of inclusion shapes are considered in this paper, but it is found that the time to coalescence does not depend strongly on shape. We leave it to future work to add these refinements and extend this type of analysis to important functional proteins such as ion-channels.[8]

Author contributions

XL carried out all numerical calculations and proofs, participated in the design of the study and drafted the manuscript. PKP conceived and designed the study and edited the manuscript. Both authors gave final approval for publication and agree to be held accountable for the work performed therein.

Conflicts of interest

There are no conflicts of interest to declare.

A Shape functions for star and rod inclusion

The shape function for star shaped inclusion of side ℓ is given by:

$$\mathscr{R}_1 = \begin{cases} \dfrac{\sqrt{3}\ell}{2}\dfrac{1}{\sin\left(\theta_1+\frac{\pi}{6}\right)}, & 0^\circ < \theta_1 \le 30^\circ, \\ \dfrac{\sqrt{3}\ell}{2}\dfrac{1}{\cos(\theta_1)}, & 30^\circ < \theta_1 \le 60^\circ, \\ \dfrac{\sqrt{3}\ell}{2}\dfrac{1}{\sin\left(\theta_1-\frac{\pi}{6}\right)}, & 60^\circ < \theta_1 \le 90^\circ, \\ \dfrac{\sqrt{3}\ell}{2}\dfrac{1}{\cos\left(\theta_1-\frac{\pi}{3}\right)}, & 90^\circ < \theta_1 \le 120^\circ, \\ \dfrac{\sqrt{3}\ell}{2}\dfrac{1}{\sin\left(\theta_1-\frac{\pi}{2}\right)}, & 120^\circ < \theta_1 \le 150^\circ, \\ \dfrac{\sqrt{3}\ell}{2}\dfrac{1}{\cos\left(\theta_1-\frac{2\pi}{3}\right)}, & 150^\circ < \theta_1 \le 180^\circ, \\ \dfrac{\sqrt{3}\ell}{2}\dfrac{1}{\sin\left(\theta_1-\frac{5\pi}{6}\right)}, & 180^\circ < \theta_1 \le 210^\circ, \\ \dfrac{\sqrt{3}\ell}{2}\dfrac{1}{\cos(\theta_1-\pi)}, & 210^\circ < \theta_1 \le 240^\circ, \\ \dfrac{\sqrt{3}\ell}{2}\dfrac{1}{\sin\left(\theta_1-\frac{7\pi}{6}\right)}, & 240^\circ < \theta_1 \le 270^\circ, \\ \dfrac{\sqrt{3}\ell}{2}\dfrac{1}{\cos\left(\theta_1-\frac{4\pi}{3}\right)}, & 270^\circ < \theta_1 \le 300^\circ, \\ \dfrac{\sqrt{3}\ell}{2}\dfrac{1}{\sin\left(\theta_1-\frac{3\pi}{2}\right)}, & 300^\circ < \theta_1 \le 330^\circ, \\ \dfrac{\sqrt{3}\ell}{2}\dfrac{1}{\cos\left(\theta_1-\frac{5\pi}{3}\right)}, & 330^\circ < \theta_1 \le 360^\circ, \end{cases} \tag{35}$$

The shape function for rod inclusion with major axis length 2ℓ and minor axis length $\frac{\sqrt{3}\ell}{2}$ is given by:

$$\mathscr{R}_1 = \begin{cases} \sqrt{3}\ell \dfrac{1}{\sin\left(\theta_1 + \frac{\pi}{3}\right)}, & 0^\circ < \theta_1 \le 30^\circ, \\ \dfrac{\sqrt{3}\ell}{2} \dfrac{1}{\sin(\theta_1)}, & 30^\circ < \theta_1 \le 150^\circ, \\ \sqrt{3}\ell \dfrac{1}{\sin\left(\theta_1 - \frac{\pi}{3}\right)}, & 150^\circ < \theta_1 \le 180^\circ, \\ \sqrt{3}\ell \dfrac{1}{\sin\left(\theta_1 - \frac{2\pi}{3}\right)}, & 180^\circ < \theta_1 \le 210^\circ, \\ \dfrac{\sqrt{3}\ell}{2} \dfrac{1}{\sin(\theta_1 - \pi)}, & 210^\circ < \theta_1 \le 330^\circ, \\ \sqrt{3}\ell \dfrac{1}{\sin\left(\theta_1 - \frac{4\pi}{3}\right)}, & 330^\circ < \theta_1 \le 360^\circ, \end{cases} \tag{36}$$

B Proof of theorem 1

Following techniques in ref. 27, 33 and 36, we integrate eqn (19) for P over all $t \ge 0$,

$$\int_0^\infty \frac{\partial P}{\partial t} \mathrm{d}t = \frac{\partial}{\partial r}\left[\frac{1}{\nu}\frac{\partial \phi}{\partial r} g_1 + D\frac{\partial g_1}{\partial r}\right] + \frac{1}{r}\left[\frac{1}{\nu}\frac{\partial \phi}{\partial r} g_1 + D\frac{\partial g_1}{\partial r}\right] \tag{37}$$

$$-\frac{1}{r}\delta(r-y) = \mathscr{L}_{\mathrm{r}} g_1(r,y), \tag{38}$$

where $\frac{1}{r}\delta(r-y)$ is the initial condition and the second order linear differential operator $\mathscr{L}_{\mathrm{r}}$: $\mathscr{D}(\mathscr{L}_{\mathrm{r}}) \subset C^2([R_1,R_2]) \to C^2([R_1,R_2])$ is defined as,

$$\mathscr{L}_{\mathrm{r}} = \frac{\partial}{\partial r}\left[\frac{1}{\nu}\frac{\partial \phi}{\partial r} + D\frac{\partial}{\partial r}\right] + \frac{1}{r}\left[\frac{1}{\nu}\frac{\partial \phi}{\partial r} + D\frac{\partial}{\partial r}\right], \tag{39}$$

with domain

$$\mathscr{D}(\mathscr{L}_{\mathrm{r}}) = \{v_1 \in C^2([R_1,R_2]) | v_1(R_1) = 0, \\ k_{\mathrm{B}}\mathrm{T} v_{1'}(R_2) + \phi'(R_2) v_1(R_2) = 0\}. \tag{40}$$

Using the method in ref. 27, we can get the adjoint operator $\mathscr{L}_{\mathrm{r}}^*$ which satisfies $\langle v_2, \mathscr{L}_{\mathrm{r}} v_1\rangle = \langle \mathscr{L}_{\mathrm{r}}^* v_2, v_1\rangle, \forall v_1 \in \mathscr{D}(\mathscr{L}_{\mathrm{r}}), v_2 \in \mathscr{D}(\mathscr{L}_{\mathrm{r}}^*)$,

$$\mathscr{L}_{\mathrm{r}}^* = -\frac{1}{\nu}\frac{\partial \phi}{\partial r}\frac{\partial}{\partial r} + D\frac{\partial^2}{\partial r^2} + \frac{1}{\nu}\frac{\partial \phi}{\partial r}\frac{1}{r} - D\frac{\partial \frac{1}{r}}{\partial r}. \tag{41}$$

with domain

$$\mathscr{D}(\mathscr{L}_{\mathrm{r}}^*) = \left\{ v_2 \in C^2([R_1,R_2]) \middle| v_2(R_1) = 0, \frac{v_2(R_2)}{R_2} - v_2'(R_2) = 0 \right\}, \tag{42}$$

and the inner product is defined as,

$$\langle v_1, v_2\rangle = \int_{R_1}^{R_2} v_1 v_2 \mathrm{d}r, \quad \forall v_1 \in \mathscr{D}(\mathscr{L}_{\mathrm{r}}), v_2 \in \mathscr{D}(\mathscr{L}_{\mathrm{r}}^*). \tag{43}$$

Proofs for the existence of the solutions of second order inhomogeneous linear ordinary differential equation are well known. Hence, we can find a $u_0 \in C^2([R_1,R_2])$ s.t. $\mathscr{L}_{\mathrm{r}}^* u_0(r) = r$. Then, it follows from eqn (23) that,

$$\begin{aligned} T_1(y) &= \int_{R_1}^{R_2} \left(\mathscr{L}_{\mathrm{r}}^* u_0(r)\right) g_1(r,y)\mathrm{d}r \\ &= \int_{R_1}^{R_2} u_0(r)(\mathscr{L}_{\mathrm{r}} g_1(r,y))\mathrm{d}r \\ &= -\int_{R_1}^{R_2} u_0(r)\frac{1}{r}\delta(r-y)\mathrm{d}r = -u_0(y)\frac{1}{y}, \end{aligned} \tag{44}$$

$$\Rightarrow \mathscr{L}_y^* y T_1(y) = -y. \tag{45}$$

Using eqn (41), we can derive eqn (25), a second order ODE for $T_1(y)$. The boundary condition of $T_1(y)$ at the absorbing wall is straightforward:[33,36] $T_1(R_1) = 0$. For the boundary condition at the reflecting wall, we appeal to the Langevin equation in eqn (27). If the particle sits at position R_2, decomposing the overdamped Langevin equation[27] into radial direction and angular direction, we have,

$$\mathrm{d}y = -\frac{1}{\nu}\frac{\partial \phi}{\partial y}\mathrm{d}t + \sqrt{\frac{2k_{\mathrm{B}}T\mathrm{d}t}{\nu}}\xi_y, \tag{46}$$

$$\mathrm{d}\theta = -\frac{1}{\nu}\frac{1}{y}\frac{\partial \phi}{\partial \theta}\mathrm{d}t + \frac{1}{y}\sqrt{\frac{2k_{\mathrm{B}}T\mathrm{d}t}{\nu}}\xi_\theta. \tag{47}$$

After time $\mathrm{d}t$, the particle can only move to $R_2 + \mathrm{d}y(\mathrm{d}y < 0)$ along the radial direction because of the reflecting wall at R_2. The motion along the angular direction can be neglected because $T_1(y)$ does not have dependence on angular direction. Note that $\mathrm{d}y$ is a random variable depending on ξ_y and $\mathrm{d}t$ with constraint $R_1 \le R_2 + \mathrm{d}y \le R_2$. Then, we can write

$$\begin{aligned} T_1(R_2) &= \mathrm{d}t + C_1(\mathrm{d}t)\int_{C_2(\mathrm{d}t)}^0 T_1(R_2+\mathrm{d}y)G(\xi_y)\mathrm{d}\xi_y \\ &= \mathrm{d}t + C_1(\mathrm{d}t)\int_{C_2(\mathrm{d}t)}^0 \left(T_1(R_2) + T_1'(R_2+\eta_{\mathrm{d}y})\mathrm{d}y\right)G(\xi_y)\mathrm{d}\xi_y \\ &= \mathrm{d}t + T_1(R_2) \\ &\quad + C_1(\mathrm{d}t)\int_{C_2(\mathrm{d}t)}^0 (T_1'(R_2) + \eta_{\mathrm{d}_y} T_1''(R_2+\beta_{\mathrm{d}_y}))\mathrm{d}y G(\xi_y)\mathrm{d}\xi_y \\ &= \mathrm{d}t + T_1(R_2) - \frac{1}{\nu}\frac{\partial \phi}{\partial y}T_1'(R_2)\mathrm{d}t \\ &\quad + C_1(\mathrm{d}t)\int_{C_2(\mathrm{d}t)}^0 T_1'(R_2)\sqrt{\frac{2k_{\mathrm{B}}T\mathrm{d}t}{\nu}}\xi_y G(\xi_y)\mathrm{d}\xi_y + C_1(\mathrm{d}t) \\ &\quad \times \int_{C_2(\mathrm{d}t)}^0 \frac{\eta_{\mathrm{d}_y}}{\mathrm{d}y} T_1''(R_2+\beta_{\mathrm{d}_y})\left(\frac{2k_{\mathrm{B}}T\mathrm{d}t}{\nu}\xi_y{}^2 + o(\mathrm{d}t)\right)G(\xi_y)\mathrm{d}\xi_y \end{aligned} \tag{48}$$

where we used mean value theorem twice to reach to eqn (49) with $R_2 + \mathrm{d}y < R_2 + \eta_{\mathrm{d}y} < R_2 + \beta_{\mathrm{d}y} < R_2$. Note that $\beta_{\mathrm{d}y}$ depends on $\eta_{\mathrm{d}y}$ and thus depends on $\mathrm{d}y$. $C_2(\mathrm{d}t)$ is the value to satisfy $R_2 + \mathrm{d}y = R_1$ for given $\mathrm{d}t$ and ξ_y. $C_1(\mathrm{d}t)$ is the scaling factor such that the integral of

probability density equals 1: $C_1(\mathrm{d}t)\int_{C_2(\mathrm{d}t)}^{0} G(\xi_y)\mathrm{d}\xi_y = 1$ where $G(\xi_y) = \frac{\mathrm{e}^{-\xi_y^2/2}}{\sqrt{2\pi}}$. After some re-arrangements and dividing by $\mathrm{d}t$ on both sides,

$$\begin{aligned} -1 = &-\frac{1}{\nu}\frac{\partial \phi}{\partial y}T_1'(R_2) + T_1'(R_2)\sqrt{\frac{2k_\mathrm{B}T}{\nu \mathrm{d}t}}C_1(\mathrm{d}t)\int_{C_2(\mathrm{d}t)}^{0}\xi_y G(\xi_y)\mathrm{d}\xi_y \\ &+ C_1(\mathrm{d}t)\int_{C_2(\mathrm{d}t)}^{0}\frac{\eta_{\mathrm{d}_y}}{\mathrm{d}y}T_1''(R_2+\beta_{\mathrm{d}_y})\left(\frac{2k_\mathrm{B}T}{\nu}\xi_y{}^2 + o(1)\right)G(\xi_y)\mathrm{d}\xi_y. \end{aligned} \tag{49}$$

As $\mathrm{d}t \to 0$, $C_1 \to 2$, $C_2 \to -\infty$. Note that $\frac{\eta_{\mathrm{d}_y}}{\mathrm{d}y} < 1$ and we have $|T_1''(R_2+\beta_{\mathrm{d}_y})| < M$ for some M because T_1 is C^2. Then if we take $t \to \infty$ the third term in RHS of eqn (49) can be bounded as,

$$\begin{aligned} &\lim_{t\to\infty}\left|C_1(\mathrm{d}t)\int_{C_2(\mathrm{d}t)}^{0}\frac{\eta_{\mathrm{d}_y}}{\mathrm{d}y}T_1''(R_2+\beta_{\mathrm{d}_y})\left(\frac{2k_\mathrm{B}T}{\nu}\xi_y{}^2+o(1)\right)G(\xi_y)\mathrm{d}\xi_y\right| \\ &\le \lim_{t\to\infty} C_1(\mathrm{d}t)\int_{-\infty}^{0}\left|\frac{\eta_{\mathrm{d}_y}}{\mathrm{d}y}T_1''(R_2+\beta_{\mathrm{d}_y})\left(\frac{2k_\mathrm{B}T}{\nu}\xi_y{}^2+o(1)\right)G(\xi_y)\right|\mathrm{d}\xi_y \\ &\le 2M\lim_{t\to\infty} C_1(\mathrm{d}t)\int_{-\infty}^{0}\left|\left(\frac{2k_\mathrm{B}T}{\nu}\xi_y{}^2\right)G(\xi_y)\right|\mathrm{d}\xi_y \\ &\le 4M\int_{-\infty}^{0}\left|\left(\frac{2k_\mathrm{B}T}{\nu}\xi_y{}^2\right)G(\xi_y)\right|\mathrm{d}\xi_y \\ &< \infty. \end{aligned} \tag{50}$$

The first term in the RHS of eqn (49) is independent of $\mathrm{d}t$ and thus is finite as $t \to \infty$. For the second term in RHS of eqn (49), $\lim_{t\to\infty}\left|C_1(\mathrm{d}t)\int_{C_2(\mathrm{d}t)}^{0}\xi_y G(\xi_y)\mathrm{d}\xi_y\right| < \infty$, but $\sqrt{\frac{2k_\mathrm{B}\mathrm{T}}{\nu \mathrm{d}t}} \to \infty$ as $\mathrm{d}t \to 0$. Since the LHS of eqn (49) is finite, we must have $T_1'(R_2) = 0$.

C Proof of theorem 2

We transform eqn (29) into polar coordinates,

$$\frac{\partial p}{\partial t} = \mathscr{F}_{r,\theta}p = \nabla \cdot S, \tag{51}$$

where the elliptic differential operator $\mathscr{F}_{r,\theta}{:}\mathscr{D}(\mathscr{F}_{r,\theta}) \subset C^2([R_1,R_2]\times[0,2\pi]) \to C^2([R_1,R_2]\times[0,2\pi])$ is in divergence form, with domain

$$\begin{aligned} \mathscr{D}(\mathscr{F}_{r,\theta}) = \Big\{ & v_1 \in C^2([R_1,R_2]\times[0,2\pi]) | v_1(R_1,\theta) = 0, \\ & \times \frac{\partial S(R_2,\theta)}{\partial r} = 0, v_1(r,0) = v_1(r,2\pi)\Big\}, \end{aligned} \tag{52}$$

and the inner product is defined as,

$$\langle v_1, v_2\rangle = \int_{R_1}^{R_2}\int_0^{2\pi} v_1 v_2 \mathrm{d}r\mathrm{d}\theta, \quad \forall v_1, v_2 \in \mathscr{D}(\mathscr{F}_{r,\theta}). \tag{53}$$

The expression of $\mathscr{F}_{r,\theta}$ can be found in ref. 27 and we ignore the expression of S for brevity. Then, it's useful to derive $\mathscr{F}_{r,\theta}^*$ (see ref. 27), the adjoint operator of $\mathscr{F}_{r,\theta}$ that satisfies $\left\langle v_1, \mathscr{F}_{r,\theta}v_2\right\rangle = \left\langle \mathscr{F}_{r,\theta}^* v_1, v_2\right\rangle, \forall v_1 \in \mathscr{D}\left(\mathscr{F}_{r,\theta}\right), v_2 \in \mathscr{D}\left(\mathscr{F}_{r,\theta}^*\right)$.

Next, we integrate eqn (51) for p over $t \ge 0$ and get,

$$-\frac{1}{r}\delta(r-y)\delta(\theta-\alpha) = \mathscr{F}_{r,\theta}q_1. \tag{54}$$

$\mathscr{F}_{r,\theta}^*$ is uniformly elliptic with certain boundary conditions the solution of which has been discussed in ref. 37. Then, we can find a $u_0 \in C^2([R_1,R_2]\times[0,2\pi])$ s.t. $\mathscr{F}_{r,\theta}^* u_0(r,\theta) = r$. It follows from eqn (30) that,

$$\begin{aligned} T_1(y,\alpha) &= \int_{R_1}^{R_2}\int_0^{2\pi} q_1\left(\mathscr{F}_{r,\theta}^* u_0(r,\theta)\right)\mathrm{d}\theta\mathrm{d}r \\ &= \int_{R_1}^{R_2}\int_0^{2\pi} u_0(r,\theta)\mathscr{F}_{r,\theta}q_1\mathrm{d}\theta\mathrm{d}r \\ &= -\int_{R_1}^{R_2}\int_0^{2\pi} u_0(r,\theta)\frac{1}{r}\delta(r-y)\delta(\theta-\alpha)\mathrm{d}\theta\mathrm{d}r \\ &= -\frac{1}{y}u_0(y,\alpha), \end{aligned} \tag{55}$$

$$\Rightarrow \mathscr{F}_{y,\alpha}^* y T_1(y,\alpha) = -y. \tag{56}$$

Then, we can derive a second order PDE for $T_1(y)$ (eqn (32)). For boundary conditions, we just need to worry about the reflecting wall. For anisotropic case, $\mathrm{d}y < 0$. $\mathrm{d}\theta$ could be either positive or negative. Similarly we can write,

$$\begin{aligned} T(R_2,\theta) = &\,\mathrm{d}t + C_1(\mathrm{d}t)\int_{C_2(\mathrm{d}t)}^{0}\int_{-\infty}^{\infty} T(R_2+\mathrm{d}y,\theta+\mathrm{d}\theta) \\ &\times G(\xi_\theta)\mathrm{d}\xi_\theta G(\xi_y)\mathrm{d}\xi_y \\ = &\,\mathrm{d}t + C_1(\mathrm{d}t)\int_{C_2(\mathrm{d}t)}^{0}\int_{-\infty}^{\infty}[T(R_2+\mathrm{d}y,\theta) \\ &+ T_\theta(R_2+\mathrm{d}y,\theta+\eta_{\mathrm{d}_y,\mathrm{d}_\theta}^*)\mathrm{d}\theta\Big]G(\xi_\theta)\mathrm{d}\xi_\theta G(\xi_y)\mathrm{d}\xi_y \\ = &\,\mathrm{d}t + C_1(\mathrm{d}t)\int_{C_2(\mathrm{d}t)}^{0}\Big[T(R_2,\theta) + T_y(R_2+\eta_{\mathrm{d}_y},\theta)\mathrm{d}y\Big]G(\xi_y)\mathrm{d}\xi_y \\ &+ C_1(\mathrm{d}t)\int_{C_2(\mathrm{d}t)}^{0}\int_{-\infty}^{\infty}\Big[T_\theta\left(R_2+\mathrm{d}y,\theta+\eta_{\mathrm{d}_y,\mathrm{d}_\theta}^*\right)\mathrm{d}\theta\Big] \\ &\times G(\xi_\theta)\mathrm{d}\xi_\theta G(\xi_y)\mathrm{d}\xi_y \\ = &\,\mathrm{d}t + C_1(\mathrm{d}t)\int_{C_2(\mathrm{d}t)}^{0}(T_y(R_2,\theta) \\ &+ \eta_{\mathrm{d}_y}T_{yy}(R_2+\beta_{\mathrm{d}_y},\theta))\mathrm{d}yG(\xi_y)\mathrm{d}\xi_y \\ &+ C_1(\mathrm{d}t)\int_{C_2(\mathrm{d}t)}^{0}\int_{-\infty}^{\infty}[T_\theta(R_2+\mathrm{d}y,\theta)\mathrm{d}\theta]G(\xi_\theta)\mathrm{d}\xi_\theta G(\xi_y)\mathrm{d}\xi_y \\ &+ C_1(\mathrm{d}t)\int_{C_2(\mathrm{d}t)}^{0}\int_{-\infty}^{\infty}\left[T_{\theta\theta}\left(R_2+\mathrm{d}y,\theta+\beta_{\mathrm{d}_y,\mathrm{d}_\theta}^*\right)(\mathrm{d}\theta)^2\frac{\eta_{\mathrm{d}_y,\mathrm{d}_\theta}{}^*}{\mathrm{d}\theta}\right] \\ &\times G(\xi_\theta)\mathrm{d}\xi_\theta G(\xi_y)\mathrm{d}\xi_y + T(R_2,\theta) \end{aligned}$$

$$
\begin{aligned}
&= \mathrm{d}t + T(R_2,\theta) + C_1(\mathrm{d}t)\int_{C_2(\mathrm{d}t)}^{0} \frac{\eta_{\mathrm{d}_y}}{\mathrm{d}y} T_{yy}(R_2+\beta_{\mathrm{d}_y},\theta) \\
&\times (\mathrm{d}y)^2 G(\xi_y)\mathrm{d}\xi_y - \frac{1}{\nu}\frac{\partial \phi}{\partial y} T_y(R_2,\theta)\mathrm{d}t \\
&+ C_1(\mathrm{d}t)\int_{C_2(\mathrm{d}t)}^{0} T_y(R_2,\theta)\sqrt{\frac{2k_{\mathrm{B}}T\mathrm{d}t}{\nu}}\xi_y G(\xi_y)\mathrm{d}\xi_y \\
&- C_1(\mathrm{d}t)\int_{C_2(\mathrm{d}t)}^{0}\int_{-\infty}^{\infty}\left[T_\theta(R_2+\mathrm{d}y,\theta)\frac{1}{\nu}\frac{1}{R_2}\frac{\partial \phi}{\partial \theta}\mathrm{d}t\right] G(\xi_\theta)\mathrm{d}\xi_\theta \\
&\times G(\xi_y)\mathrm{d}\xi_y + C_1(\mathrm{d}t)\int_{C_2(\mathrm{d}t)}^{0}\int_{-\infty}^{\infty}\left[T_{\theta\theta}\left(R_2+\mathrm{d}y,\theta+\beta^*_{\mathrm{d}_y,\mathrm{d}_\theta}\right)\right. \\
&\left.\times\left(\frac{2k_{\mathrm{B}}T\mathrm{d}t}{R_2^2\nu}\xi_\theta^2 + o(\mathrm{d}t)\right)\frac{\eta^*_{\mathrm{d}_y,\mathrm{d}_\theta}}{\mathrm{d}\theta}\right] G(\xi_\theta)\mathrm{d}\xi_\theta G(\xi_y)\mathrm{d}\xi_y \\
&+ C_1(\mathrm{d}t)\int_{C_2(\mathrm{d}t)}^{0} T_\theta(R_2+\mathrm{d}y,\theta)\frac{1}{R_2}\sqrt{\frac{2k_{\mathrm{B}}T\mathrm{d}t}{\nu}} \\
&\times\int_{-\infty}^{\infty}\xi_\theta G(\xi_\theta)\mathrm{d}\xi_\theta G(\xi_y)\mathrm{d}\xi_y,
\end{aligned}
\tag{57}
$$

where in the process to eqn (57) we used mean value theorem three times with $\theta < \theta + \beta^*_{\mathrm{d}_y,\mathrm{d}_\theta} < \theta + \eta^*_{\mathrm{d}_y,\mathrm{d}_\theta} < \theta + \mathrm{d}\theta$ if $\mathrm{d}\theta > 0$ and $\theta + \mathrm{d}\theta < \theta + \eta^*_{\mathrm{d}_y,\mathrm{d}_\theta} < \theta + \beta^*_{\mathrm{d}_y,\mathrm{d}_\theta} < \theta$ if $\mathrm{d}\theta < 0$. After some re-arrangements and dividing by $\mathrm{d}t$ on both sides, we get

$$
\begin{aligned}
-1 &= C_1(\mathrm{d}t)\int_{C_2(\mathrm{d}t)}^{0}\frac{\eta_{\mathrm{d}_y}}{\mathrm{d}y}T_{yy}(R_2+\beta_{\mathrm{d}_y},\theta)\left(\frac{2k_{\mathrm{B}}T}{\nu}\xi_y^2 + o(1)\right)G(\xi_y)\mathrm{d}\xi_y \\
&+ C_1(\mathrm{d}t)\int_{C_2(\mathrm{d}t)}^{0} T_y(R_2,\theta)\sqrt{\frac{2k_{\mathrm{B}}T}{\nu\mathrm{d}t}}\xi_y G(\xi_y)\mathrm{d}\xi_y - \frac{1}{\nu}\frac{\partial \phi}{\partial y}T_y(R_2,\theta) \\
&- C_1(\mathrm{d}t)\int_{C_2(\mathrm{d}t)}^{0}\left[T_\theta(R_2+\mathrm{d}y,\theta)\frac{1}{\nu}\frac{1}{R_2}\frac{\partial \phi}{\partial \theta}\right]G(\xi_y)\mathrm{d}\xi_y \\
&+ C_1(\mathrm{d}t)\int_{C_2(\mathrm{d}t)}^{0}\int_{-\infty}^{\infty}\left[T_{\theta\theta}\left(R_2+\mathrm{d}y,\theta+\beta^*_{\mathrm{d}_y,\mathrm{d}_\theta}\right)\left(\frac{2k_{\mathrm{B}}T}{\nu R_2^2}\xi_\theta^2 + o(1)\right)\right. \\
&\left.\times\frac{\eta^*_{\mathrm{d}_y,\mathrm{d}_\theta}}{\mathrm{d}\theta}\right]G(\xi_\theta)\mathrm{d}\xi_\theta G(\xi_y)\mathrm{d}\xi_y + C_1(\mathrm{d}t)\int_{C_2(\mathrm{d}t)}^{0} T_\theta(R_2+\mathrm{d}y,\theta) \\
&\times\frac{1}{R_2}\sqrt{\frac{2k_{\mathrm{B}}T}{\nu\mathrm{d}t}}\int_{-\infty}^{\infty}\xi_\theta G(\xi_\theta)\mathrm{d}\xi_\theta G(\xi_y)\mathrm{d}\xi_y.
\end{aligned}
\tag{58}
$$

Using the continuity of T_θ, T_{yy} and $T_{\theta\theta}$ and the fact that $\frac{\eta_{\mathrm{d}_y}}{\mathrm{d}y}, \frac{\eta^*_{\mathrm{d}_y,\mathrm{d}_\theta}}{\mathrm{d}\theta} < 1$, it is clear that the 1st, 3rd, 4th, 5th terms on RHS of eqn (58) are finite as $\mathrm{d}t \to 0$. The 6th term is vanishing due to $\int_{-\infty}^{\infty}\xi_\theta G(\xi_\theta)\mathrm{d}\xi_\theta = 0$. Since the LHS of eqn (58) is finite also, the 2nd term on RHS of eqn (58) must also be finite as $\mathrm{d}t \to 0$. Accordingly, $T_y(R_2,\theta) = 0$ follows from $\lim_{\mathrm{d}t\to\infty}\sqrt{\frac{2k_{\mathrm{B}}T}{\nu\mathrm{d}t}} \to \infty$.

Acknowledgements

We acknowledge support for this work through an NSF grant CMMI 1662101.

References

1 R. Matthews and C. N. Likos, *J. Phys. Chem. B*, 2013, **117**, 8283–8292.
2 B. J. Reynwar, G. Illya, V. A. Harmandaris, M. M. Müller, K. Kremer and M. Deserno, *Nature*, 2007, **447**, 461.
3 T. Ruiz-Herrero and M. F. Hagan, *Biophys. J.*, 2015, **108**, 585–595.
4 R. Golestanian, M. Goulian and M. Kardar, *Phys. Rev. E: Stat., Nonlinear, Soft Matter Phys.*, 1996, **54**, 6725.
5 K. Kim, J. Neu and G. Oster, *Biophys. J.*, 1998, **75**, 2274–2291.
6 O. Kahraman, P. D. Koch, W. S. Klug and C. A. Haselwandter, *Sci. Rep.*, 2016, **6**, 19214.
7 C. A. Haselwandter and R. Phillips, *PLoS Comput. Biol.*, 2013, **9**, e1003055.
8 C. A. Haselwandter and R. Phillips, *EPL*, 2013, **101**, 68002.
9 N. Dan, P. Pincus and S. Safran, *Langmuir*, 1993, **9**, 2768–2771.
10 H. Aranda-Espinoza, A. Berman, N. Dan, P. Pincus and S. Safran, *Biophys. J.*, 1996, **71**, 648–656.
11 T. Ursell, K. C. Huang, E. Peterson and R. Phillips, *PLoS Comput. Biol.*, 2007, **3**, e81.
12 E. B. Lindgren, I. N. Derbenev, A. Khachatourian, H.-K. Chan, A. J. Stace and E. Besley, *J. Chem. Theory Comput.*, 2018, **14**, 905–915.
13 C. Yolcu, R. C. Haussman and M. Deserno, *Adv. Colloid Interface Sci.*, 2014, **208**, 89–109.
14 R. Bradley and R. Radhakrishnan, *Polymers*, 2013, **5**, 890–936.
15 H. Agrawal, L. Liu and P. Sharma, *Soft Matter*, 2016, **12**, 8907–8918.
16 C. Huang, H. Yuan and S. Zhang, *Appl. Phys. Lett.*, 2011, **98**, 043702.
17 H. Li and G. Lykotrafitis, *Phys. Rev. E: Stat., Nonlinear, Soft Matter Phys.*, 2015, **92**, 012715.
18 M. M. Müller and M. Deserno, *Prog. Theor. Phys. Suppl.*, 2010, **184**, 351–363.
19 Y. Schweitzer and M. M. Kozlov, *PLoS Comput. Biol.*, 2015, **11**, e1004054.
20 C. Yolcu, I. Z. Rothstein and M. Deserno, *EPL*, 2011, **96**, 20003.
21 W. Helfrich, *Z. Naturforsch., C: J. Biosci.*, 1973, **28**, 693–703.
22 R. Phillips and P. Rob, *Crystals, defects and microstructures: modeling across scales*, Cambridge University Press, 2001.
23 A. V. Shnyrova, J. Ayllon, I. I. Mikhalyov, E. Villar, J. Zimmerberg and V. A. Frolov, *J. Cell Biol.*, 2007, **179**, 627–633.
24 D. Rower, M. Padidar and P. J. Atzberger, 2019, arXiv preprint arXiv:1906.01146.
25 E. Schäffer and U. Thiele, *Eur. Phys. J. E: Soft Matter Biol. Phys.*, 2004, **14**, 169–175.

26 C. Tozzi, N. Walani and M. Arroyo, *New J. Phys.*, 2019, **21**, 093004.
27 X. Liao and P. K. Purohit, *J. Mech. Phys. Solids*, 2020, **135**, 103787.
28 J. W. Klingelhoefer, T. Carpenter and M. S. Sansom, *Biophys. J.*, 2009, **96**, 3519–3528.
29 X. Liang and P. K. Purohit, *J. Mech. Phys. Solids*, 2016, **90**, 29–44.
30 X. Liang and P. K. Purohit, *Extreme Mech. Lett.*, 2018, **18**, 29–35.
31 X. Periole, T. Huber, S.-J. Marrink and T. P. Sakmar, *J. Am. Chem. Soc.*, 2007, **129**, 10126–10132.
32 R. Phillips, T. Ursell, P. Wiggins and P. Sens, *Nature*, 2009, **459**, 379–385.
33 H. Risken, *The Fokker-Planck Equation*, Springer, 1996, pp. 63–95.
34 S. Itô, *et al.*, *Duke Math. J.*, 1957, **24**, 299–312.
35 T. T. Hormel, S. Q. Kurihara, M. K. Brennan, M. C. Wozniak and R. Parthasarathy, *Phys. Rev. Lett.*, 2014, **112**, 188101.
36 D. T. Gillespie, *Markov processes: an introduction for physical scientists*, Elsevier, 1991.
37 A. V. Bitsadze, *Boundary value problems for second order elliptic equations*, Elsevier, 2012, vol. 5.

